Modelling and simulation of ductile failure in textured aluminium alloys subjected to compression-tension loading

Bjørn Håkon Frodal[a,b,*], Lars Edvard Blystad Dæhli[a], Tore Børvik[a,b], Odd Sture Hopperstad[a,b]

[a] *Structural Impact Laboratory (SIMLab), Department of Structural Engineering, Norwegian University of Science and Technology (NTNU), NO-7491, Trondheim, Norway*
[b] *Centre for Advanced Structural Analysis (CASA), NTNU, NO-7491, Trondheim, Norway*

Abstract

The effects of strain path change on the ductile failure process of textured aluminium alloys are investigated through reversed loading experiments and finite element-based unit cell simulations. Three extruded aluminium alloys (AA6060, AA6082.25 and AA6082.50) are solution heat-treated and artificially aged to three different conditions, namely temper O (annealed), temper T7 (overaged) and temper T6 (peak strength). Compression-tension experiments on diabolo-shaped specimens are conducted including five different pre-compression levels (0, 10, 20 30, 40%), i.e., the specimens are first compressed to a prescribed strain and then reloaded to fracture in tension. The materials are modelled with an advanced plasticity model accounting for plastic anisotropy, non-associated plastic flow, nonlinear isotropic and kinematic hardening, strength differential effect, and transient and permanent effects of strain path change. Crystal plasticity finite element analyses are performed to determine the plastic anisotropy of the materials and then used to calibrate the anisotropic yield surfaces, whereas the work-hardening response is calibrated from the experimental data. The effects of grain morphology and precipitate structure on the plastic anisotropy are neglected. Finite element simulations of all the reversed loading tests are performed and the non-proportional loading history from the centre of the specimen is extracted. These non-proportional loading histories are imposed to a unit cell model with a central spherical particle to study the effect of pre-compression on the ductile failure process, where the initial plastic anisotropy and the work-hardening behaviour after strain path change are accounted for. The strain to coalescence of the three-dimensional unit cell is mapped back to the reversed loading tests to determine the logarithmic strain to failure after the strain path change, and the numerical results are compared with the experimental data. The unit cell model predicts an approximately constant tensile ductility with pre-compression for the different materials. Variations are observed between the materials as the strength, work hardening and anisotropy are found to influence the response of the unit cell differently and affect the tensile ductility after the pre-deformation. In the experiments, the tensile ductility is largely constant or exhibits a small increase for the majority of the materials, but for some alloy-temper combinations a larger increase is observed, which is not captured in the unit cell computations.

Keywords: A. Ductility, A. Fracture, B. Crystal plasticity, C. Finite elements, Unit cell modelling

1. Introduction

The different microstructural characteristics of metals, such as grain structure and crystallographic texture, determine their plastic behaviour. Rolled plates and extruded profiles typically exhibit plastic anisotropy, which should be modelled by an anisotropic yield criterion. Numerous anisotropic yield criteria have been proposed in the literature. Hill (1948) proposed a quadratic yield function for orthotropic materials, which gives reasonable predictions for traditional steels. For aluminium alloys, the Hill yield criterion

*Corresponding author
Email address: bjorn.h.frodal@ntnu.no (Bjørn Håkon Frodal)

has been found to provide less accurate estimates of the yield surface (Woodthorpe and Pearce, 1970; Stout et al., 1983; Iadicola et al., 2008). Barlat et al. (1991) proposed a yield criterion for orthotropic materials, using linear transformation of the stress tensor. This criterion was based on the non-quadratic yield function of Hershey (1954) and Hosford (1972), which gives good prediction of the yield surface for isotropic materials. Karafillis and Boyce (1993) further generalised the theory of linear transformations to describe a more universal anisotropic yield function, as to also accommodate other material symmetries. Later, Bron and Besson (2004) introduced an additional linear transformation in the yield criterion of Karafillis and Boyce (1993) to increase the number of anisotropy coefficients and the degree of flexibility. Barlat et al. (2005) proposed a new criterion based on the non-quadratic yield criterion of Barlat et al. (1991) using two linear transformations, consisting of 16 independent anisotropy coefficients (Van Den Boogaard et al., 2016) for the most general formulation. More recently, anisotropic yield criteria including even more linear transformations have been introduced (Aretz et al., 2010; Aretz and Barlat, 2013). Yield criteria based on invariants of the stress tensor have also been extended to anisotropy by implementing linear transformations of the stress tensor (e.g., Cazacu and Barlat, 2001; Yoshida et al., 2013; Lou and Yoon, 2018).

The improved flexibility and accuracy of these yield functions come at the cost of more anisotropy coefficients that have to be determined. The calibration process then becomes challenging as more experimental tests are required. It is therefore desirable to determine the material behaviour of complex materials without performing extensive experimental testing, which is both expensive and time consuming. To reduce the number of experimental tests needed to calibrate the yield surface of a material, virtual material testing based on crystal plasticity theory can be utilised. This can be done in two ways. The first approach is to use virtual testing in combination with experiments to provide data for deformation modes that are difficult to obtain experimentally (Barlat et al., 2005; Grytten et al., 2008; Zhang et al., 2015). In the second approach, only virtual testing is used to determine the yield surface of a material (Saai et al., 2013; Zhang et al., 2015; Zhang et al., 2016). The accuracy of such methods relies on the capability of the crystal plasticity theory to incorporate the important microstructural effects and also the flexibility of the phenomenological yield function.

The full-constraint Taylor model (Taylor, 1938; Bishop and Hill, 1951a,b) is one of the most used representations to describe the response of polycrystals. This approach is based on the assumption that all grains in an aggregate experience the same deformation; thus, compatibility is fulfilled but stress equilibrium is violated. Owing to this violation, several relaxed-constraint Taylor models have been proposed in an attempt to develop a more realistic description of polycrystals, while keeping the simplicity of the full-constraint Taylor model (Kocks and Chandra, 1982; Van Houtte, 1982, 1988; Van Houtte et al., 2002). Another way of representing a polycrystalline aggregate is by so-called self-consistent models. In these models, each grain is represented by an ellipsoidal inclusion surrounded by a homogeneous equivalent medium. The most popular version of the self-consistent models seems to be the visco-plastic self-consistent (VPSC) model (Hutchinson, 1976; Molinari et al., 1987; Lebensohn and Tomé, 1993, 1994). Unlike the Taylor model, the self-consistent models satisfy both stress equilibrium and deformation compatibility. In contrast, the shape of grains, their local interaction and inhomogeneities of the mechanical fields within grains are not accounted for (Lebensohn et al., 2012; Zhang et al., 2016).

More recently, full-field micromechanical approaches such as the combination of crystal plasticity with the finite element method (CP-FEM) (Raabe and Roters, 2004; Kanjarla et al., 2010; Saai et al., 2013; Zhang et al., 2015) or a spectral method using fast Fourier transformation (FFT) (Lebensohn et al., 2012; Eisenlohr et al., 2013; Zhang et al., 2016) have become increasingly popular with the advances in computer technology. These methods typically require more computational resources than the various Taylor and self-consistent models, but are capable of accounting for stress equilibrium and compatibility across grain boundaries, local interaction and inhomogeneities of the mechanical fields within grains, and resolving the complex grain morphology of polycrystalline materials. The FFT is more computational efficient in solving the mechanical problem, but is limited to periodic boundary conditions (Zhang et al., 2016). In contrast, CP-FEM requires more computational resources, but can be used to solve the mechanical response of a polycrystalline material with any geometry and boundary conditions. Currently, the CP-FEM framework is restricted to the mesoscopic scale as numerical simulations of structural components and full structures are too computationally demanding, and for such large-scale problems phenomenological plasticity models

are still preferred.

By utilising hierarchical modelling schemes, it is possible to combine the accuracy of the polycrystal plasticity models with the computational efficiency of the phenomenological plasticity models. Barlat et al. (2005) combined experimental data and results obtained with the VPSC model to calibrate the Yld2004-18p yield surface for an aluminium sheet material. Grytten et al. (2008) determined the parameters of the same yield function using (i) only experimental data, (ii) only virtual data obtained with the full-constraint Taylor model, and (iii) a combination of these two methods. They found that the full-constraint Taylor model was not capable of reproducing the experimental results, and that the yield surface determined from experimental data only was favourable. Saai et al. (2013) compared the full-constraint Taylor model to CP-FEM simulations utilising the hierarchical modelling framework. They found that the yield surface calibrated solely from CP-FEM predicted the experimental data quite accurately, while the full-constraint Taylor model gave less accurate results. Zhang et al. (2015) compared five different homogenisation models, including full-constraint and relaxed-constraint Taylor models, the VPSC model and CP-FEM, and concluded that CP-FEM was one of the methods that gave the best agreement with the experimental data. These identification methods have also been used to calibrate different yield functions, or used with different crystal plasticity models (Inal et al., 2010; An et al., 2011; Zhang et al., 2016).

One of the advantages of the crystal plasticity theory is its ability to predict the change of plastic anisotropy by evolving the crystallographic texture, and it can thus account for anisotropic hardening. Anisotropic hardening has also been introduced in phenomenological yield criteria. The first attempts to include this feature were made by introducing an interpolation method to determine the evolution of the yield surface with plastic deformation (Plunkett et al., 2007; Aretz, 2008). Gawad et al. (2015) presented a hierarchical multi-scale framework that accounts for evolution of the plastic anisotropy by systematically recalibrating the yield surface to data provided by the crystal plasticity virtual experiment framework. Kohar et al. (2017) accounted for microstructure evolution by introducing the plastic spin into the phenomenological plasticity framework, where the evolution of the plastic spin was calibrated based on crystal plasticity. Lee et al. (2017) proposed a model describing the evolution of the yield surface by coupling quadratic and non-quadratic yield functions with a non-associated flow rule.

After a strain path change, materials typically experience a transient response. The Bauschinger effect (Bauschinger, 1881) is often observed after reversed loading, where the re-yielding stress after the strain path change is lower than the flow stress prior to unloading, and the subsequent work-hardening rate is, in general, much higher than under monotonic loading. Another transient effect is work-hardening stagnation, which is observed after the first transient phase. The work-hardening rate temporarily decreases, making a plateau in the flow stress curve, before it increases again with straining. These transient effects will commonly vanish after a certain plastic strain, and the flow stress curve after the strain path change coalesces with the flow stress curve for monotonic loading (Ha et al., 2013). In contrast, some materials experience permanent softening after the strain path change. In this case, the flow stress curve after strain path change remains lower than the monotonic flow stress curve, although the work-hardening rate may reach the same level as under monotonic loading (Li and Bate, 1991; Mánik et al., 2015).

Two main approaches exist for including the effects of strain path change in phenomenological plasticity models. The first approach relies on combined isotropic and kinematic hardening, incorporating internal variables with a fading memory of the strain path. The yield surface of the material translates, expands and shrinks with plastic deformation, whereas its shape is invariant. This approach was first proposed by Teodosiu and Hu (1995), and their model applies second and fourth order tensors to describe the transient response. More recently, Mánik et al. (2015) proposed a model including only second order tensors to describe the behaviour after strain path change. This model, denoted the MHH model, is not only capable of describing the transients, but also the permanent softening unlike the model of Teodosiu and Hu (1995). In the second approach, the effects of strain path changes are accounted for by distortion of the yield surface. This yield surface distortion has been observed experimentally during both proportional and non-proportional loading paths (Khan et al., 2009, 2010a,b; Pandey et al., 2013). François (2001) introduced a "distorted stress" tensor into the yield function to describe an egg-shaped distortion of the yield surface. Based on two-dimensional rheological ideas, Shutov et al. (2011), and Shutov and Ihlemann (2012) proposed models that account for yield surface distortion. Freund et al. (2012) introduced a model based on one-

dimensional constitutive equations with only scalar variables to describe the distortion of the yield surface. A general model, called the Homogeneous Anisotropic Hardening (HAH) model, capable of distorting any homogeneous yield surface was proposed by Barlat et al. (2011). This model accounts for the Bauschinger effect without the use of kinematic hardening. Later, several extensions and enhancements have been made to this model to account for more complex effects of strain path changes (Barlat et al., 2013, 2014; Ha et al., 2013; Lee et al., 2015; Qin et al., 2017). An evaluation of the HAH and MHH models was recently performed by Qin et al. (2017). They observed that for one of the materials investigated, the MHH model gave better agreement with experimental data after a single strain path change for large pre-strains, while the HAH model gave better agreement after a double strain path change. Recently, Qin et al. (2018) proposed a distortional yield surface model that combines some of the features of the HAH model with the MHH model. Strain path change models have also been proposed and used within the crystal plasticity framework (e.g., Holmedal et al., 2008; Kitayama et al., 2013; Wen et al., 2015, 2016).

For certain metallic materials, a strength differential effect, i.e., a higher flow stress in compression than in tension, can be observed. Several studies have observed the strength differential effect in aluminium alloys (e.g., Spitzig and Richmond, 1984; Bai and Wierzbicki, 2008; Luo and Rousselier, 2014; Holmen et al., 2017). Spitzig and Richmond (1984) suggested that the strength differential effect and the pressure sensitivity they observed for aluminium were linked to the effect of hydrostatic pressure on dislocation motion. Bulatov et al. (1999) performed atomistic simulations of aluminium, and examined the lattice resistance to dislocation motion under pressure. The results support the conclusion by Spitzig and Richmond (1984) suggesting that pressure-dependent slip in aluminium is caused by the interaction of a transient activation dilatancy of the moving dislocations with pressure. Along with pressure sensitivity, Bai and Wierzbicki (2008) explicitly included the influence of the third deviatoric stress invariant in simulations of an AA2024-T351 aluminium alloy. More recently, Luo and Rousselier (2014) accounted for the strength differential effect of an extruded aluminium alloy by introducing initial backstresses on the slip system level utilising crystal plasticity. A strength differential effect was observed along the transverse direction of the extruded profile, whereas the tensile and compressive yield stresses were identical along the extrusion direction. Holmen et al. (2017) investigated four aluminium alloys in several different tempers exhibiting the strength differential effect. Based on the work by Spitzig and Richmond (1984), a pressure dependent non-associative Drucker and Prager (1952) plasticity model was calibrated, and good agreement was found between the numerical and experimental data. For more elaborate discussions regarding the strength differential effect in aluminium alloys the reader is referred to, e.g., Luo and Rousselier (2014) and Holmen et al. (2017).

Research on ductile fracture has mainly addressed proportional loading conditions, whereas ductile failure in real applications is typically preceded by a non-proportional loading path. Recently, the important influence of non-proportional loading has been investigated both experimentally (Bao and Treitler, 2004; Kristoffersen et al., 2013; Papasidero et al., 2015; Marcadet and Mohr, 2015; Basu and Benzerga, 2015; Frodal et al., 2017) and numerically using unit cells (Zhang and Skallerud, 2010; Benzerga et al., 2012; Kristoffersen et al., 2016; Dæhli et al., 2016a). During non-proportional loading, the transient and permanent effects of strain path change are essential to the description and prediction of ductile failure. Effects such as work-hardening stagnation may lead to an earlier localisation of plastic deformation and can have a detrimental effect on ductility.

Reversed loading is an important type of non-proportional loading, and has been studied in more recent years in the context of ductile failure (Bao and Treitler, 2004; Kristoffersen et al., 2013; Papasidero et al., 2015; Marcadet and Mohr, 2015; Frodal et al., 2017). Kristoffersen et al. (2013) investigated the effect of pre-compression on the ductility of an X65 steel used in offshore pipelines. They used diabolo-shaped specimens and performed experimental tests with pre-compression of up to 100%. For a pre-compression of 10% the tensile ductility increased compared to monotonic tension, whereas for higher levels the ductility decreased with pre-compression. Marcadet and Mohr (2015) evaluated the response of a dual phase steel sheet, using reversed loading experiments and numerical simulations of the tests. In the finite element simulations, they included the effects of transients such as the Bauschinger effect and work-hardening stagnation, and observed that the local thickening of the sheet during compression delayed the formation of a neck and the consequent increase in stress triaxiality. The experiments performed on notched flat specimens using a floating anti-buckling device showed that the strain to failure increased with pre-compression. For an aluminium alloy,

Bao and Treitler (2004) performed reversed loading experiments on diabolo-shaped specimens. They used three different specimen geometries to account for different triaxiality levels during the reversed loading tests, and found that the tensile ductility of the material decreased with pre-compression in all the tests. The reduced tensile ductility was attributed to particle fracture and an increased dislocation density after the pre-loading, which accelerated the nucleation, growth and coalescence of voids in the succeeding tension stage. Papasidero et al. (2015) performed experiments on tubular specimens involving torsion, compression and tension tests in different combinations to study the effect of stress state and loading path on the onset of ductile fracture in aluminium. The experiments with non-proportional loading paths showed a pronounced effect of the loading path on the strain to failure. Frodal et al. (2017) investigated the influence of pre-compression on three extruded aluminium alloys with different microstructure and strength. Reversed loading experiments conducted on diabolo-shaped specimens showed that pre-compression had a marked influence on the ductility of the alloys, and the effect was significantly different between them.

Unit cell modelling is an important tool for studying ductile failure, either by proportional or non-proportional loading. Zhang and Skallerud (2010) investigated the effects of pre-strain on void coalescence using axisymmetric unit cell analyses. They imposed non-proportional loading histories on the unit cell consisting of a pre-strain stage in uniaxial tension, before a tensile stage with an elevated stress triaxiality ratio was applied and compared with results for proportional loading paths. Benzerga et al. (2012) performed analyses of an axisymmetric unit cell subjected to different proportional and non-proportional loading paths. Dæhli et al. (2016a) extracted the non-proportional loading paths from smooth axisymmetric tensile tests and applied them in analyses using an axisymmetric unit cell. These simulations were compared with analyses using proportional loading paths, given by the strain-average triaxiality to material failure. Results from these studies clearly demonstrate the importance of non-proportional loading in the context of ductile failure predictions. Kristoffersen et al. (2016) used axisymmetric unit cell analyses of reversed loading tests with diabolo-shaped specimens. A non-proportional loading path was created by two proportional loading steps, one in compression and one in the subsequent tension stage.

The effect of plastic anisotropy on ductile failure has also been studied with unit cell calculations. Benzerga and Besson (2001) were the first to account for anisotropy in terms of a Hill (1948) matrix formulation under proportional loading. Chien et al. (2001) and Wang et al. (2004) carried out three-dimensional (3D) unit cell simulations with the same anisotropic yield criterion. Steglich et al. (2010) assessed the ductile failure properties of an aluminium alloy using 3D unit cell calculations, where the yield criterion of Bron and Besson (2004) was employed. The individual and coupled effects of void shape and material anisotropy were studied by Keralavarma and Benzerga (2010) and Keralavarma et al. (2011) using axisymmetric unit cells. Recently, Dæhli et al. (2017) performed 3D unit cell analyses for a wide range of stress states applying the yield criterion of Barlat et al. (2005) for the matrix material. The full-constraint Taylor method was used to determine the yield surfaces representing typical crystallographic textures for face centred cubic (FCC) metals. Legarth and Tvergaard (2018) studied the interaction between plastic anisotropy, initial void shape and void spacing and their effect on void growth applying 3D unit cell simulations.

The aim of the present paper is to study the ductile failure process of textured aluminium alloys during reversed loading by experimental tests and three-dimensional unit cell simulations. First, an experimental programme is presented involving reversed loading tests of diabolo-shaped specimens on three aluminium alloys (AA6060, AA6082.25 and AA6082.50) solution heat-treated and artificially aged to three conditions, namely temper O (annealed), temper T7 (overaged) and temper T6 (peak strength). Second, finite element simulations of all the tests are conducted, using an advanced plasticity model to describe the material behaviour as outlined below. Third, unit cell simulations are carried out to study the ductile failure mechanisms numerically, where the non-proportional loading history is obtained from the finite element simulations of the tests. The results from the unit cell simulations are further mapped back to the reversed loading tests of the diabolo-shaped specimen, and compared to the experimental results. In order to incorporate the plastic anisotropy of the materials, the anisotropic yield criterion Yld2004-18p (Barlat et al., 2005) is applied in all simulations. CP-FEM calculations are used to determine the shape of the yield surface, incorporating the effect of the work-hardening behaviour of each material. The strength differential effect observed in the experimental tests is accounted for by using a pressure-dependent version of the Yld2004-18p yield criterion

and a non-associated flow rule to retain isochoric plastic flow. The work hardening is described by combined isotropic and kinematic hardening, while additional internal variables are used to account for transient and permanent effects of strain path change (Mánik et al., 2015). A two-step process is adopted to calibrate the work-hardening rules based on experimental data from selected tests.

2. Materials

In this paper, the three aluminium alloys AA6060, AA6082.25 and AA6082.50 are investigated. The chemical composition of the alloys is given in Table 1. These alloys were provided by Hydro Aluminium as extruded rectangular profiles with a thickness of 10 mm and a width of 83 mm. Prior to the solution heat-treatment, diabolo-shaped specimens were machined from the extruded profiles (Frodal et al., 2017). The specimens were then solution heat-treated and artificially aged to three different tempers, namely temper O (annealed), temper T7 (overaged) and temper T6 (peak strength).

Table 1: Chemical compositions of the aluminium alloys in wt%.

Alloy	Fe	Si	Mg	Mn	Cr	Cu	Zn	Ti	Al
AA6060	0.193	0.422	0.468	0.015	0.000	0.002	0.005	0.008	Bal.
AA6082.25	0.180	0.880	0.600	0.530	0.150	0.020	0.005	0.011	Bal.
AA6082.50	0.200	1.020	0.670	0.540	0.001	0.003	0.005	0.010	Bal.

The heat-treatment was performed in five stages. Stage 1-3 consisted of keeping the specimens in a salt bath at 540 °C for 15 min, water quenching, and storage in room temperature for 15 min. In stage 4, the specimens were kept in an oil bath at 185 °C for either five hours to achieve temper T6, or for one week to achieve temper T7. To attain temper O, the specimens were kept in a salt bath at 350 °C for 24 hours. Stage 5 consisted of air-cooling to room temperature.

The three aluminium alloys have different grain structure and texture. The AA6060 alloy has a recrystallised grain structure comprising equi-axed grains, and exhibits a cube texture with a minor Goss component. A typical fibrous, non-recrystallised grain structure is observed for the AA6082.25 alloy, which has a cube texture with orientations along the β-fibre. The AA6082.50 alloy has recrystallised grain structure with large elongated grains and a rotated cube texture. For further details about the materials, the reader is referred to Khadyko et al. (2014) and Frodal et al. (2017).

3. Experiments

3.1. Experimental procedures

Reversed loading tests were performed to study the influence of pre-compression on the ductility of the three alloys in different tempers. Diabolo-shaped specimens were used in the tests, with a minimum diameter of 6.4 mm and a notch radius of 3.6 mm. The specimens were machined from the extruded profiles, oriented along the transverse direction (TD).

A displacement-controlled test machine with a constant cross-head velocity of 0.50 mm/min was used to perform the tests. Using an in-house measuring system, the minimum diameters along the extrusion direction (ED) and thickness direction (ND) of the specimens were continuously measured until fracture (Frodal et al., 2017).

The current area of the minimum cross-section can be estimated as an elliptical area by

$$A = \frac{\pi}{4} D_1 D_3 \tag{1}$$

where D_1 and D_3 are the measured diameters in ED and ND, respectively. The true stress over the minimum cross-section area is then

$$\sigma_t = \frac{F}{A} \tag{2}$$

where F is the measured force. Assuming plastic incompressibility and negligible elastic strains, the logarithmic strain is given by

$$\varepsilon_l = \ln\left(\frac{A_0}{A}\right) \tag{3}$$

where A_0 is the initial cross-section area of the specimen. It is important to note that σ_t and ε_l represent average values over the minimum cross-section area of the specimen. Note also that close to failure this strain measure, based on the assumption of plastic incompressibility, becomes less accurate due to damage-induced increase of the porosity.

For each alloy and temper, the specimens were subjected to five different levels of pre-compression. The specimens were first compressed to a predefined strain level of either 0, 10, 20, 30 or 40% pre-compression, and then pulled to fracture in tension. Two or three tests were conducted for each pre-compression level. Fracture surfaces of the failed specimens were investigated in a Zeiss Gemini Supra 55VP FESEM operated at 20 kV.

Note that the test results for the three alloys in temper T6 have previously been presented in Frodal et al. (2017) and are included here for completeness. For further details about the experimental setup, the reader is referred to Frodal et al. (2017).

3.2. Experimental results

3.2.1. Stress-strain curves

Figure 1 presents the stress-strain curves from the reversed loading tests in terms of true stress and logarithmic strain. The point of failure is indicated by a cross for each stress-strain curve. This is defined as either the point where a marked drop in the load level occurs, or where a distinct change in the slope of the stress-strain curve is observed. In the tests of the AA6060 alloy in temper O subjected to 40% pre-compression, failure occured in the threaded section of the specimen due to severe work hardening in the notch during compression, and the results from these tests are omitted. Table 2 presents the yield stress at 0.2% plastic strain in tension and compression, in addition to the re-yielding stress after load reversal. Note that the stress level is amplified by the triaxial stress field in the notched area of the specimen. For the three alloys in temper T7 and T6, the re-yielding stresses are lower than the initial yield stress, whereas for temper O the re-yielding stresses are higher than the initial yield stress. The re-yielding stress increases with increasing pre-compression for the AA6060 and AA6082.50 alloys in all tempers, as well as for the AA6082.25 alloy in temper O. In contrast, the AA6082.25 alloy in temper T7 and T6 has an almost constant re-yielding stress with increasing pre-compression.

For all the materials, a strength differential effect is observed, i.e., the initial yield stress and the flow stress at small plastic strains are markedly higher in compression than in tension, see Table 2. A more comprehensive investigation of the strength differential effect for the materials used in the present study can be found in Holmen et al. (2017).

Table 2: Yield stresses at 0.2% plastic strain, $\sigma_{0.2}$, and re-yielding stresses after pre-compression, with standard deviations.

Material	Tension (MPa)	Compression (MPa)	Re-yielding after 10% pre-compression (MPa)	Re-yielding after 20% pre-compression (MPa)	Re-yielding after 30% pre-compression (MPa)	Re-yielding after 40% pre-compression (MPa)
AA6060-O	42.5 ± 0.9	-44.2 ± 1.4	82.5 ± 1.9	89.2 ± 0.4	94.0 ± 0.5	-
AA6060-T7	162.7 ± 1.3	-169.8 ± 2.0	136.5 ± 0.2	144.9 ± 1.6	148.2 ± 1.8	148.3 ± 0.8
AA6060-T6	207.0 ± 4.7	-221.4 ± 5.8	184.7 ± 5.6	187.6 ± 9.2	195.4 ± 5.5	201.8 ± 4.3
AA6082.25-O	81.0 ± 0.1	-83.3 ± 0.7	107.3 ± 0.6	115.7 ± 0.8	117.5 ± 0.2	117.8 ± 0.8
AA6082.25-T7	216.0 ± 1.8	-217.7 ± 2.4	163.3 ± 1.5	166.2 ± 0.7	167.0 ± 2.0	169.7 ± 1.0
AA6082.25-T6	362.7 ± 10.2	-381.6 ± 7.0	272.9 ± 3.5	269.2 ± 6.4	269.6 ± 3.9	269.1 ± 6.1
AA6082.50-O	41.7 ± 1.4	-46.9 ± 1.4	86.0 ± 1.4	94.6 ± 2.0	101.3 ± 0.6	111.2 ± 6.9
AA6082.50-T7	248.7 ± 2.2	-262.3 ± 5.8	179.0 ± 0.5	183.2 ± 1.4	189.1 ± 4.0	189.2 ± 0.6
AA6082.50-T6	356.3 ± 13.5	-391.6 ± 8.9	283.7 ± 1.2	305.1 ± 2.8	315.1 ± 5.7	315.8 ± 8.1

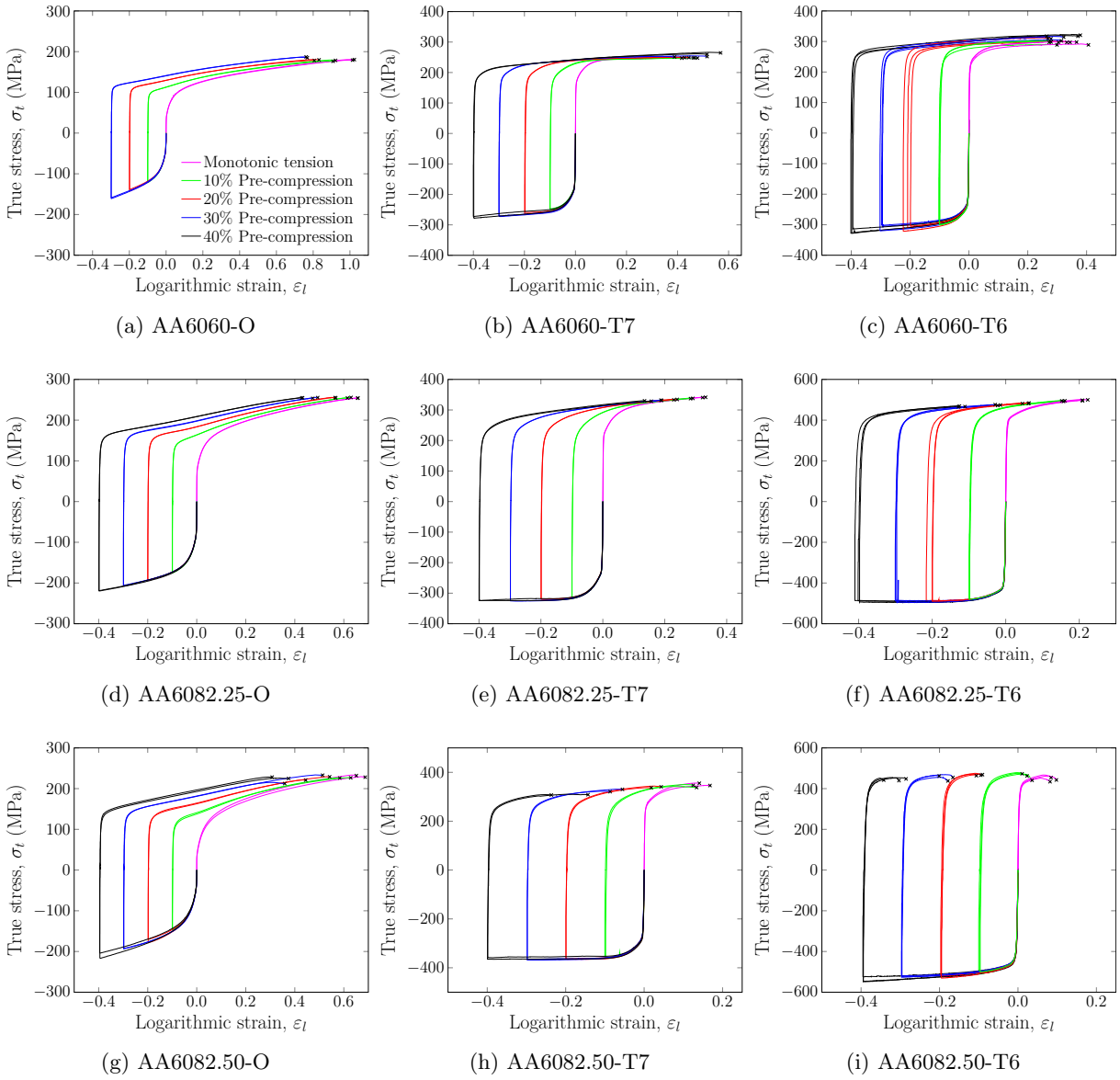

(a) AA6060-O (b) AA6060-T7 (c) AA6060-T6

(d) AA6082.25-O (e) AA6082.25-T7 (f) AA6082.25-T6

(g) AA6082.50-O (h) AA6082.50-T7 (i) AA6082.50-T6

Figure 1: Stress-strain curves for the three alloys in different tempers. The point of failure is indicated with a cross.

After load reversal, the Bauschinger effect is observed, see Figure 1, and is seen to be largest in the tests subjected to 10% pre-compression for all the materials. At larger pre-compression levels, the Bauschinger effect decreases with increasing pre-compression. The materials also exhibit permanent softening after load reversal, as the magnitude of the flow stress is substantially reduced. Permanent softening is discussed in further detail in Section 5.3. Work-hardening stagnation is observed after re-yielding for the three alloys in temper O. The effect is greatest for the tests subjected to 10% pre-compression, and then it decreases with increasing pre-compression and almost disappears after 40% pre-compression. The work-hardening stagnation can be explained by the pile-up of dislocations around obstacles during plastic deformation, which experience less resistance when travelling in the opposite direction after load reversal (Hasegawa et al., 1986). The reason why work-hardening stagnation is observed for the O temper and not for the others is probably the large non-shearable precipitates present in this temper.

The measured Lankford coefficients in tension, compression and in tension after load reversal are presented in Table 3. These coefficients give the ratio between the incremental strain in ED and ND, and thus the evolution of the cross-section of the specimen. The Lankford coefficients are different in tension and compression as well as between the different alloys and tempers. For the AA6060 and AA6082.50 alloys, the Lankford coefficients are greater in compression than in tension, while they are similar and closer to unity for the AA6082.25 alloy. Small variations are observed between different tempers. In tension after pre-compression, a small difference and evolution of the Lankford coefficients with pre-compression is observed. In general, the coefficients for the AA6060 and AA6082.25 alloys suggest that the materials become more anisotropic with increasing pre-compression, although this effect is modest, while for the AA6082.50 alloy the evolution of the Lankford coefficient is more irregular.

Table 3: Measured Lankford coefficients in tension, compression and in tension after pre-compression, with standard deviations.

Material	Tension	Compression	In tension after 10% pre-compression	In tension after 20% pre-compression	In tension after 30% pre-compression	In tension after 40% pre-compression
AA6060-O	1.24 ± 0.01	1.40 ± 0.06	1.35 ± 0.03	1.48 ± 0.01	1.63 ± 0.03	-
AA6060-T7	1.24 ± 0.01	1.27 ± 0.09	1.32 ± 0.01	1.35 ± 0.01	1.43 ± 0.02	1.47 ± 0.01
AA6060-T6	1.27 ± 0.01	1.36 ± 0.10	1.35 ± 0.01	1.37 ± 0.04	1.43 ± 0.05	1.50 ± 0.13
AA6082.25-O	0.82 ± 0.01	0.85 ± 0.03	0.82 ± 0.00	0.80 ± 0.01	0.78 ± 0.01	0.74 ± 0.01
AA6082.25-T7	0.85 ± 0.01	0.83 ± 0.02	0.84 ± 0.01	0.84 ± 0.01	0.83 ± 0.01	0.81 ± 0.01
AA6082.25-T6	0.97 ± 0.01	0.95 ± 0.02	0.96 ± 0.01	0.94 ± 0.01	0.93 ± 0.00	0.91 ± 0.01
AA6082.50-O	0.45 ± 0.05	0.51 ± 0.07	0.41 ± 0.05	0.33 ± 0.04	0.36 ± 0.02	0.26 ± 0.03
AA6082.50-T7	0.41 ± 0.06	0.59 ± 0.09	0.37 ± 0.05	0.46 ± 0.03	0.39 ± 0.01	0.43 ± 0.01
AA6082.50-T6	0.36 ± 0.05	0.55 ± 0.05	0.45 ± 0.04	0.45 ± 0.05	0.38 ± 0.05	0.42 ± 0.08

3.2.2. Effect of pre-compression on ductility

Figure 2 presents the failure strain, ε_f, and the relative failure strain, ε_r, versus pre-compression level, where the relative failure strain is defined as $\varepsilon_r = \varepsilon_f - \varepsilon_0$ and ε_0 is the strain at load reversal. The failure strain ε_f is seen to decrease with increasing pre-compression for most of the materials. For the AA6060 alloy in temper T7 and T6, the point of failure occurred within a narrow range of strain values for different levels of pre-compression, and the failure strain is approximately constant.

The tensile ductility is here defined as the deformation capability of the material subsequent to the pre-deformation, i.e., tensile ductility is defined in terms of the relative failure strain, ε_r. Figure 2 shows that the AA6060 alloy in temper T7 and T6 and the AA6082.25 alloy in temper T7 exhibit a marked increase in tensile ductility with increasing pre-compression level. The relative failure strain is almost doubled after 40% pre-compression compared to monotonic tension for these materials. The AA6082.25 in temper O is also seen to have a relatively large increase in tensile ductility with increasing pre-compression level. The remaining materials either display a small increase in the tensile ductility or a largely constant tensile ductility with increasing pre-compression level.

It is apparent that the magnitude of the failure strain varies between the materials, and that the strength of the material plays an important role. Figure 3 shows the failure strain in monotonic tension versus the initial yield stress at 0.2% plastic strain, and it is evident that the failure strain decreases with increasing yield strength. In previous studies on various aluminium alloys, it has also been found that the failure strain tends to decrease linearly with increasing strength for similar microstructures (e.g., Lloyd, 2003; Westermann et al., 2014; Pedersen et al., 2015; Hannard et al., 2016).

3.2.3. Fracture surfaces

Figure 4 presents a selection of the most interesting fracture surfaces, namely the fracture surfaces of the AA6060 and AA6082.50 alloys in tempers O and T7 subjected to monotonic tension, whereas the fracture surfaces of the three alloys in temper T6 can be found in Frodal et al. (2017). In general, the fracture surfaces of specimens in tempers T7 and T6 for a given alloy are similar, while specimens in temper O

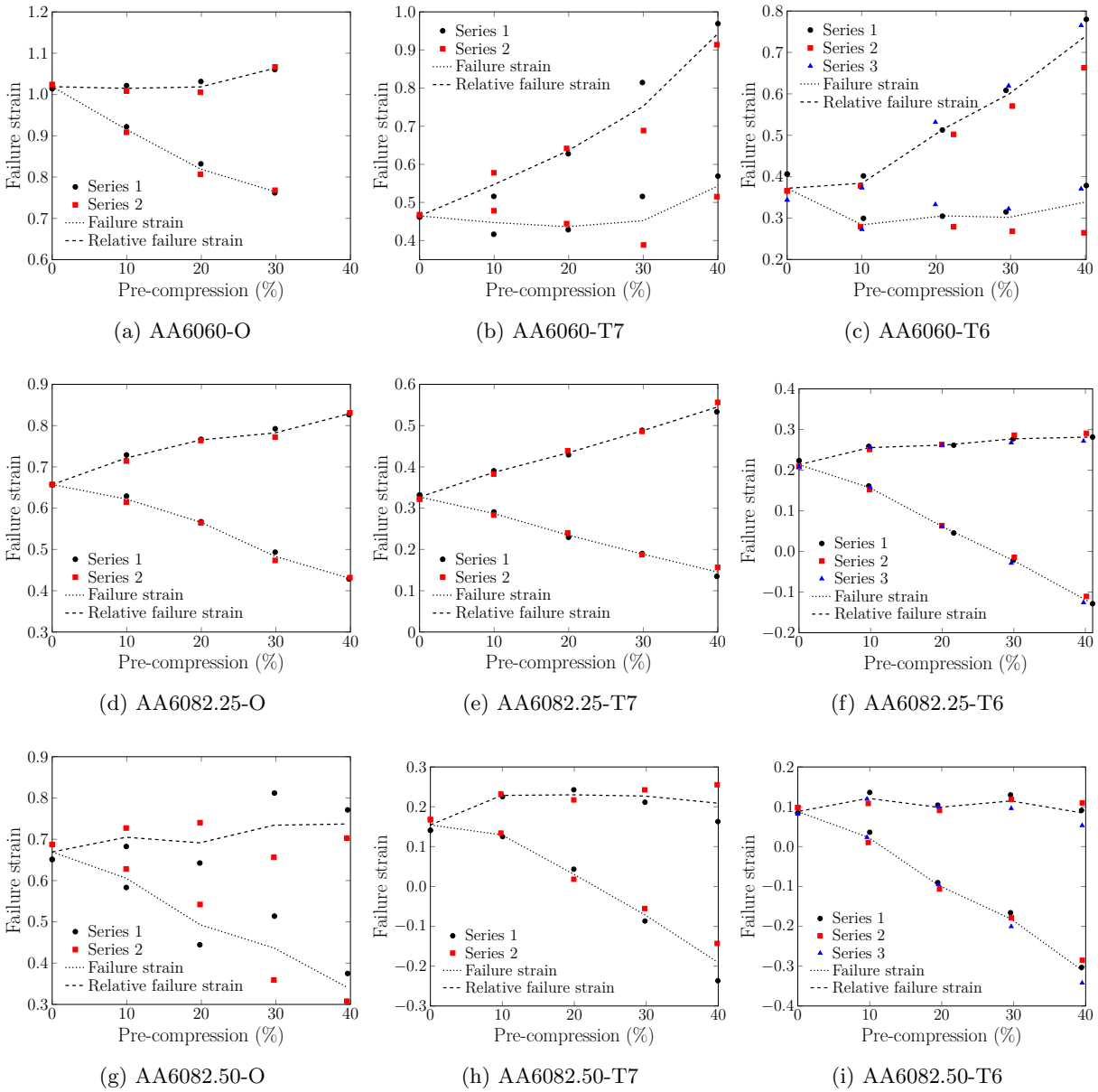

(a) AA6060-O (b) AA6060-T7 (c) AA6060-T6

(d) AA6082.25-O (e) AA6082.25-T7 (f) AA6082.25-T6

(g) AA6082.50-O (h) AA6082.50-T7 (i) AA6082.50-T6

Figure 2: Failure strain, ε_f, and relative failure strain, ε_r, versus pre-compression level for the three alloys in different tempers. The relative failure strain is the strain to failure measured with respect to the compressed configuration.

exhibit a different fracture surface. For all tempers, the specimens of the AA6060 alloy display diamond-shaped cup-and-cone fracture surfaces. The diamond shape observed for tempers T7 and T6 is similar, but is sharper than for temper O. The specimens of the AA6082.25 alloy have typical circular cup-and-cone fracture surfaces similar for all tempers. The specimens of the AA6082.50 alloy in temper O exhibit an elliptical cup-and-cone fracture surface, while in tempers T7 and T6 a shear failure mode is found for this alloy. Note that the area calculation in Equation (1) is based on an elliptical shape of the minimum cross-section area, and thus errors will be introduced at large strains for the AA6060 alloy due to the diamond-shaped minimum cross-section area. A detailed discussion of this issue can be found in Frodal et al. (2017).

The general trend is that the same failure modes and fracture surface shapes are observed with increasing pre-compression as for monotonic tension. The fracture areas become larger with increasing pre-compression

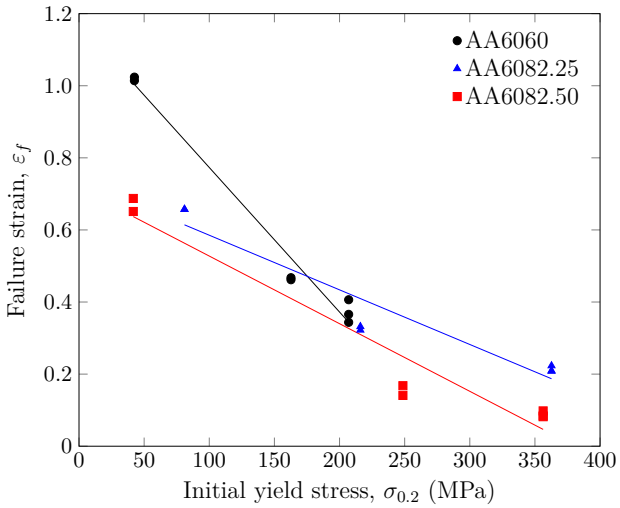

Figure 3: Failure strain, ε_f, versus initial yield stress, $\sigma_{0.2}$, for the three alloys in different tempers subjected to monotonic tension. Lines represent a linear least-square fit to the experimental data.

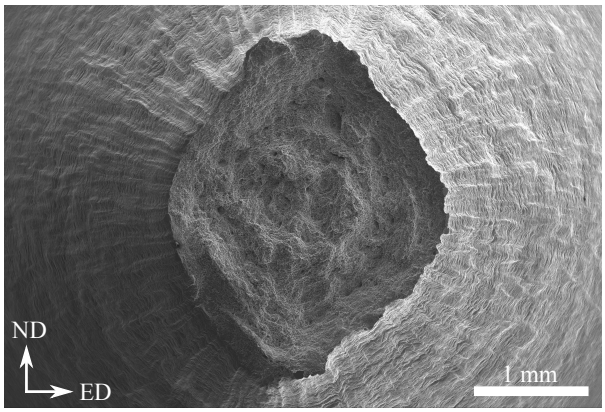

(a) AA6060-O

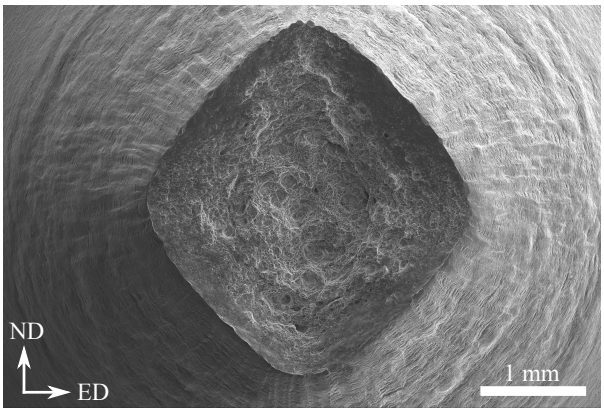

(b) AA6060-T7

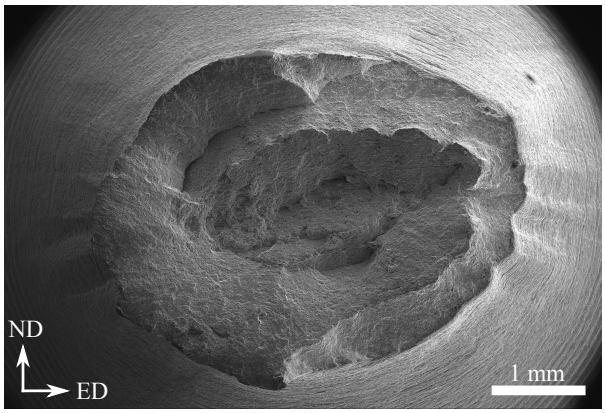

(c) AA6082.50-O

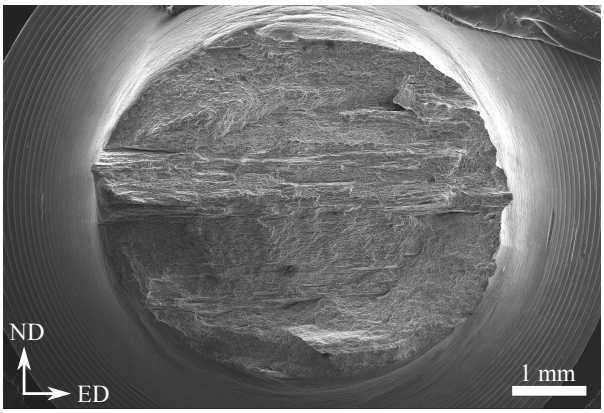

(d) AA6082.50-T7

Figure 4: Fracture surfaces of the AA6060 and AA6082.50 alloys in temper O and T7, subjected to monotonic tension.

in agreement with a lower failure strain. The only exception is the AA6060 alloy in temper T7 and T6. As the pre-compression increases, the fracture surfaces for these materials become more elliptical than the clear diamond shape observed for monotonic tension, and the area of the fracture surface is almost unchanged.

For the AA6060 alloy in temper T6, Frodal et al. (2017) observed some areas of intercrystalline fracture, and the amount was seen to decrease with increasing pre-compression. The same trend is also observed for temper T7, but fewer areas are seen than for temper T6. In contrast, intercrystalline fracture is not observed for temper O.

4. Constitutive modelling

In the finite element simulations of the material tests and in the subsequent unit cell simulations, an advanced plasticity model is applied. The anisotropic yield criterion of the plasticity model is calibrated based on polycrystal plasticity calculations. In the following, the crystal plasticity model is described first and then the phenomenological plasticity model is outlined.

4.1. Crystal plasticity

4.1.1. Single crystal plasticity

A rate-dependent crystal plasticity formulation is adopted where plastic deformation is assumed to occur by plastic slip on certain crystallographic slip systems, determined by the crystal structure. It is further assumed that the elastic deformations are infinitesimal, while the plastic deformations and rotations may be finite. For details beyond this section on general theory of single crystal plasticity, the reader is referred to the textbook of Khan and Huang (1995).

The velocity gradient $\mathbf{L}$ is additively decomposed into a symmetric and a skew-symmetric part

$$L_{ij} = D_{ij} + W_{ij} \tag{4}$$

where $\mathbf{D}$ is the symmetric rate of deformation tensor and $\mathbf{W}$ is the skew-symmetric spin tensor. These tensors are additively decomposed into elastic and plastic parts

$$D_{ij} = D^e_{ij} + D^p_{ij}, \qquad W_{ij} = W^e_{ij} + W^p_{ij} \tag{5}$$

where $\mathbf{D}^e$ and $\mathbf{D}^p$ are the elastic and plastic rate of deformation tensors, respectively. The elastic spin tensor $\mathbf{W}^e$ consists of an infinitesimal elastic contribution and rigid spin of the crystal lattice, whereas $\mathbf{W}^p$ is the plastic spin tensor caused by plastic slip. Plastic slip occurs on certain crystallographic slip systems, and the plastic parts of the rate of deformation and spin tensors are given by

$$D^p_{ij} = \frac{1}{2}\sum_{\alpha=1}^{N} \dot{\gamma}^{(\alpha)}\left(S^{(\alpha)}_{ij} + S^{(\alpha)}_{ji}\right) \tag{6}$$

$$W^p_{ij} = \frac{1}{2}\sum_{\alpha=1}^{N} \dot{\gamma}^{(\alpha)}\left(S^{(\alpha)}_{ij} - S^{(\alpha)}_{ji}\right) \tag{7}$$

where N is the number of slip systems and $\dot{\gamma}^{(\alpha)}$ is the plastic slip rate on slip system α. Further, $\mathbf{S}^{(\alpha)} = \mathbf{m}^{(\alpha)} \otimes \mathbf{n}^{(\alpha)}$ is the Schmid tensor, where $\mathbf{m}^{(\alpha)}$ and $\mathbf{n}^{(\alpha)}$ are unit vectors defining the slip direction and slip plane normal, respectively.

Let $\mathbf{e}_i, (i = 1, 2, 3)$, denote the basis for the global coordinate system, and $\hat{\mathbf{e}}_i$ the basis for a co-rotated coordinate system that rotates with the crystal lattice. The rotation of the lattice is given by the orthogonal rotation tensor $\mathfrak{R}$, that evolves according to the differential equations

$$\dot{\mathfrak{R}}_{ij} = W^e_{ik}\mathfrak{R}_{kj} \tag{8}$$

The unit vectors $\mathbf{m}^{(\alpha)}$ and $\mathbf{n}^{(\alpha)}$ are not affected by the crystallographic slip and are given by

$$m_i^{(\alpha)} = \mathfrak{R}_{ij}\hat{m}_j^{(\alpha)}, \quad n_i^{(\alpha)} = \mathfrak{R}_{ij}\hat{n}_j^{(\alpha)} \tag{9}$$

where the vector components $\hat{m}_i^{(\alpha)}$ and $\hat{n}_i^{(\alpha)}$ in the co-rotational coordinate system are constant and defined by the crystal structure.

In the co-rotated coordinate system, the rate form of the generalized Hooke's law can be expressed as

$$\dot{\hat{\sigma}}_{ij} = \hat{C}_{ijkl}\hat{D}^e_{kl} \tag{10}$$

where $\boldsymbol{\sigma}$ is the Cauchy stress tensor, and the fourth-order elasticity tensor $\boldsymbol{C}$ is assumed invariant of plastic deformation and constant in the co-rotational lattice frame. The elasticity tensor accounts for the elastic anisotropy of the crystal, and is defined by the three independent elastic constants $\hat{c}_{11}$, $\hat{c}_{12}$ and $\hat{c}_{44}$. In this case, Equation (10) can be written on matrix form as

$$\begin{bmatrix} \dot{\hat{\sigma}}_{11} \\ \dot{\hat{\sigma}}_{22} \\ \dot{\hat{\sigma}}_{33} \\ \dot{\hat{\sigma}}_{12} \\ \dot{\hat{\sigma}}_{23} \\ \dot{\hat{\sigma}}_{31} \end{bmatrix} = \begin{bmatrix} \hat{c}_{11} & \hat{c}_{12} & \hat{c}_{12} & 0 & 0 & 0 \\ \hat{c}_{12} & \hat{c}_{11} & \hat{c}_{12} & 0 & 0 & 0 \\ \hat{c}_{12} & \hat{c}_{12} & \hat{c}_{11} & 0 & 0 & 0 \\ 0 & 0 & 0 & \hat{c}_{44} & 0 & 0 \\ 0 & 0 & 0 & 0 & \hat{c}_{44} & 0 \\ 0 & 0 & 0 & 0 & 0 & \hat{c}_{44} \end{bmatrix} \begin{bmatrix} \hat{D}^e_{11} \\ \hat{D}^e_{22} \\ \hat{D}^e_{33} \\ 2\hat{D}^e_{12} \\ 2\hat{D}^e_{23} \\ 2\hat{D}^e_{31} \end{bmatrix} \tag{11}$$

The plastic power per unit volume is defined as

$$\dot{w}^p = \sigma_{ij}D^p_{ij} = \hat{\sigma}_{ij}\hat{D}^p_{ij} = \sum_{\alpha=1}^{N} \tau^{(\alpha)}\dot{\gamma}^{(\alpha)} \tag{12}$$

where the resolved shear stress $\tau^{(\alpha)}$ acting on slip system α is defined as power conjugate to the plastic slip rate $\dot{\gamma}^{(\alpha)}$. The resolved shear stresses are here defined by

$$\tau^{(\alpha)} = \sigma_{ij}S_{ij}^{(\alpha)} = \hat{\sigma}_{ij}\hat{S}_{ij}^{(\alpha)} \tag{13}$$

In this work, the plastic flow is described by the rate-dependent constitutive relation (Hutchinson, 1976)

$$\dot{\gamma}^{(\alpha)} = \dot{\gamma}_0 \left| \frac{\tau^{(\alpha)}}{\tau_c^{(\alpha)}} \right|^{\frac{1}{m}} \operatorname{sgn}(\tau^{(\alpha)}) \tag{14}$$

where $\dot{\gamma}_0$ is the reference shearing rate, m is the instantaneous strain rate sensitivity, and $\tau_c^{(\alpha)}$ is the critical resolved shear stress on slip system α. The critical resolved shear stresses, with initial value τ_0, evolve according to (Saai et al., 2013)

$$\dot{\tau}_c^{(\alpha)} = \theta(\Gamma) \sum_{\beta=1}^{N} q_{\alpha\beta} \left| \dot{\gamma}^{(\beta)} \right| \tag{15}$$

where $q_{\alpha\beta}$ is the latent hardening matrix, and $\theta(\Gamma)$ is the work-hardening rate; a function of the accumulated plastic shear strain, Γ, defined as

$$\Gamma = \int_0^t \sum_{\alpha=1}^{N} |\dot{\gamma}^{(\alpha)}| dt \tag{16}$$

The work-hardening rate is given by (Saai et al., 2013)

$$\theta(\Gamma) = \sum_{k=1}^{N_\tau} \theta_{\tau k} \exp\left(- \frac{\theta_{\tau k}}{\tau_k}\Gamma \right) \tag{17}$$

where N_τ is the number of hardening terms, and $\theta_{\tau k}$ and τ_k are the initial hardening rate and saturated value of hardening term k, respectively.

4.1.2. Polycrystal plasticity

In this work, the crystal plasticity finite element method (CP-FEM) is used to model the material anisotropy. The material is represented by a representative volume element (RVE), see Section 5.1, where each grain is explicitly modelled and behaves according to the single crystal plasticity model, described in Section 4.1.1. Thus, stress equilibrium and compatibility across grain boundaries are fulfilled. Every grain is given an initial orientation based on the crystallographic texture of the aluminium alloys, see Frodal et al. (2017) for the orientation distribution functions (ODFs).

The volume-average Cauchy stress tensor, $\bar{\boldsymbol{\sigma}}$, and the volume-average plastic power per unit volume, $\dot{\bar{w}}^p$, of the RVE are defined as

$$\bar{\boldsymbol{\sigma}} = \sum_{k=1}^{N_{\text{int}}} v_k \boldsymbol{\sigma}_k, \quad \dot{\bar{w}}^p = \sum_{k=1}^{N_{\text{int}}} v_k \dot{w}_k^p \tag{18}$$

where v_k is the volume fraction, $\boldsymbol{\sigma}_k$ is the Cauchy stress tensor, and $\dot{w}_k^p$ is the plastic power per unit volume of integration point k. The total number of integration points is N_{int}. When the initial volume of each integration point is equal, and under the assumption of infinitesimal elastic strains, the volume fraction of every integration point can be approximated by $v_k = {}^1/_{N_{\text{int}}}$.

4.2. Phenomenological plasticity

In this section, the constitutive relations of the phenomenological plasticity model are outlined. The plasticity model consists of a pressure-sensitive version of the anisotropic yield criterion Yld2004-18p (Barlat et al., 2005) to describe plastic anisotropy and the strength differential effect, a non-associated flow rule to ensure isochoric plastic flow, nonlinear isotropic and kinematic work-hardening rules, and internal variables to account for the effects of strain path changes (Mánik et al., 2015).

Again a co-rotational formulation is used, analogous to Equation (8), but under the assumption of zero plastic spin. The co-rotated Cauchy stress rate and the elastic rate of deformation tensors are related by the generalised Hooke's law, Equation (10). Elastic isotropy is assumed, and the fourth-order elasticity tensor $\boldsymbol{C}$ contains only two independent parameters, i.e., Young's modulus E and Poisson's ratio ν.

To describe the strength differential effect observed in the experimental tests, we formulate a pressure-sensitive yield criterion valid for plastic anisotropy. To this end, the Drucker and Prager (1952) yield criterion is adopted with the equivalent stress defined by the Yld2004-18p yield function (Barlat et al., 2005). Note that the pressure sensitivity is assumed to be weak. Thus, the yield criterion is formulated as

$$\Phi(\boldsymbol{\eta}, p) \equiv \phi(\boldsymbol{\eta}) - \sigma_y(p) = 0 \quad , \quad \phi(\boldsymbol{\eta}) = \frac{\varphi(\boldsymbol{\eta}) + \alpha \boldsymbol{\eta} : \boldsymbol{I}}{1 + \alpha} \tag{19}$$

where $\boldsymbol{\eta} = \boldsymbol{\sigma} - \boldsymbol{\chi}$ is the effective stress tensor, $\boldsymbol{\chi}$ is the backstress tensor, $\boldsymbol{I}$ is the second-order identity tensor, $\sigma_y(p)$ controls the size of the elastic domain, p is the accumulated plastic strain, $\varphi(\boldsymbol{\eta})$ is the equivalent stress with respect to the effective stress defined by the Yld2004-18p yield function, and α governs the pressure sensitivity. For $\alpha = 0$ the yield criterion reduces to the pressure independent Yld2004-18p yield criterion.

The equivalent stress of the anisotropic Yld2004-18p yield function is given by (Barlat et al., 2005)

$$\varphi(\boldsymbol{\eta}) = \left(\frac{1}{4} \sum_{k=1}^{3} \sum_{l=1}^{3} \left| S_k' - S_l'' \right|^a \right)^{\frac{1}{a}} \tag{20}$$

where a is an exponent determining the curvature of the yield surface, and S_k' and S_l'' are the principal values of the tensors $\boldsymbol{s}'$ and $\boldsymbol{s}''$, respectively. The tensors $\boldsymbol{s}'$ and $\boldsymbol{s}''$ are determined by the linear transformations

$$\hat{s}_{ij}' = \hat{C}_{ijkl}' \hat{s}_{kl}, \quad \hat{s}_{ij}'' = \hat{C}_{ijkl}'' \hat{s}_{kl} \tag{21}$$

where the fourth order tensors $\boldsymbol{C}'$ and $\boldsymbol{C}''$ contain coefficients describing the plastic anisotropy, and $\boldsymbol{s}$ is the deviatoric part of the effective stress tensor given as

$$\hat{s}_{ij} = \hat{\eta}_{ij} - \frac{1}{3} \hat{\eta}_{kk} \delta_{ij} \tag{22}$$

where δ_{ij} is the Kronecker delta. For an orthotropic material, Equation (21) can be written on matrix form as

$$\begin{bmatrix} \hat{s}'_{11} \\ \hat{s}'_{22} \\ \hat{s}'_{33} \\ \hat{s}'_{12} \\ \hat{s}'_{23} \\ \hat{s}'_{31} \end{bmatrix} = \begin{bmatrix} 0 & -\hat{c}'_{12} & -\hat{c}'_{13} & 0 & 0 & 0 \\ -\hat{c}'_{21} & 0 & -\hat{c}'_{23} & 0 & 0 & 0 \\ -\hat{c}'_{31} & -\hat{c}'_{32} & 0 & 0 & 0 & 0 \\ 0 & 0 & 0 & \hat{c}'_{44} & 0 & 0 \\ 0 & 0 & 0 & 0 & \hat{c}'_{55} & 0 \\ 0 & 0 & 0 & 0 & 0 & \hat{c}'_{66} \end{bmatrix} \begin{bmatrix} \hat{s}_{11} \\ \hat{s}_{22} \\ \hat{s}_{33} \\ \hat{s}_{12} \\ \hat{s}_{23} \\ \hat{s}_{31} \end{bmatrix} \tag{23}$$

$$\begin{bmatrix} \hat{s}''_{11} \\ \hat{s}''_{22} \\ \hat{s}''_{33} \\ \hat{s}''_{12} \\ \hat{s}''_{23} \\ \hat{s}''_{31} \end{bmatrix} = \begin{bmatrix} 0 & -\hat{c}''_{12} & -\hat{c}''_{13} & 0 & 0 & 0 \\ -\hat{c}''_{21} & 0 & -\hat{c}''_{23} & 0 & 0 & 0 \\ -\hat{c}''_{31} & -\hat{c}''_{32} & 0 & 0 & 0 & 0 \\ 0 & 0 & 0 & \hat{c}''_{44} & 0 & 0 \\ 0 & 0 & 0 & 0 & \hat{c}''_{55} & 0 \\ 0 & 0 & 0 & 0 & 0 & \hat{c}''_{66} \end{bmatrix} \begin{bmatrix} \hat{s}_{11} \\ \hat{s}_{22} \\ \hat{s}_{33} \\ \hat{s}_{12} \\ \hat{s}_{23} \\ \hat{s}_{31} \end{bmatrix} \tag{24}$$

where the 18 anisotropy parameters $\hat{c}'_{ij}$ and $\hat{c}''_{ij}$ together with the exponent a determine the shape of the yield surface in stress space. Recently, Van Den Boogaard et al. (2016) showed that the 18 anisotropy parameters can be reduced to 16 independent ones. Thus, we will select $\hat{c}'_{12} = \hat{c}'_{13} = 1$. Any other choice will give equivalent results, but for an isotropic material these selected values will result in that all $\hat{c}'_{ij}$ and $\hat{c}''_{ij}$ become equal to one.

By studying the strength differential effect and pressure sensitivity in aluminium, Spitzig and Richmond (1984) found that the plastic dilatancy described by the associated flow rule for a pressure sensitive yield criterion greatly overestimated their experimental findings and that the plastic volume changes were negligible in comparison. Following their work, the flow rule is assumed to be non-associated and given by

$$\hat{D}^p_{ij} = \dot{\lambda} \frac{\partial \varphi}{\partial \hat{\eta}_{ij}} \tag{25}$$

where $\dot{\lambda}$ is the plastic multiplier. The equivalent plastic strain rate is defined by the plastic power, where $\varphi(\boldsymbol{\eta})$ is taken to be power conjugate to $\dot{p}$, so that

$$\dot{p} \equiv \frac{\hat{\eta}_{ij} \hat{D}^p_{ij}}{\varphi(\boldsymbol{\eta})} = \dot{\lambda} \tag{26}$$

To obtain the latter equality, it was used that $\varphi(\boldsymbol{\eta})$ is a homogeneous function of order one with respect to the effective stress.

The backstress tensor $\boldsymbol{\chi}$ is defined as a sum of N_χ kinematic hardening terms, viz.

$$\hat{\chi}_{ij} = \sum_{k=1}^{N_\chi} \hat{\chi}^{(k)}_{ij} \tag{27}$$

Each partial hardening term $\boldsymbol{\chi}^{(k)}$ evolves according to (Armstrong and Frederick, 1966; Frederick and Armstrong, 2007)

$$\dot{\hat{\chi}}^{(k)}_{ij} = \theta_{\chi k} \left(\frac{\hat{\eta}_{ij}}{\phi(\boldsymbol{\eta})} - \frac{\hat{\chi}^{(k)}_{ij}}{Q_{\chi k}} \right) \dot{p} \tag{28}$$

where $\theta_{\chi k}$ and $Q_{\chi k}$ are parameters governing the kinematic hardening of the material.

The size of the elastic domain is given by

$$\sigma_y(p) = \sigma_0 + R(p) + R_r(p) + S_r(p) \tag{29}$$

where σ_0 is the initial yield stress, $R(p)$ is the isotropic hardening contribution for monotonic loading, $R_r(p)$ accounts for permanent softening after load reversal, and $S_r(p)$ represents the extra strength contribution

due to the built-up microstructure anisotropy during straining before load reversal. The isotropic hardening contribution for monotonic loading is given by the extended Voce hardening rule (Voce, 1948)

$$R(p) = \sum_{k=1}^{N_V} Q_{Rk}\left(1 - \exp\left(-\frac{\theta_{Rk}}{Q_{Rk}}p\right)\right) \tag{30}$$

where N_V is the number of hardening terms, and Q_{Rk} and θ_{Rk} are parameters controlling the shape of the isotropic hardening curve for monotonic loading. The evolution equations for the internal variables R_r and S_r are given by (Mánik et al., 2015)

$$\dot{R}_r = k_r \min\left(\hat{P}_{ij}\hat{N}_{ij}, 0\right)\dot{p} \tag{31}$$

$$\dot{S}_r = -c_r\left[S_r + q_r\left(\sigma_0 + R + R_r\right)\min\left(\hat{P}_{ij}\hat{N}_{ij}, 0\right)\right]\dot{p} \tag{32}$$

where k_r is a parameter controlling the permanent softening, $\boldsymbol{P}$ is the "delayed pointer", $\boldsymbol{N}$ is the direction of the plastic rate of deformation, and c_r and q_r are parameters controlling the extra strength contributions represented by S_r. The "delayed pointer" evolves according to

$$\dot{\hat{P}}_{ij} = c_p\left(\hat{N}_{ij} - \hat{P}_{ij}\right)\dot{p} \quad , \quad \hat{N}_{ij} = \frac{\hat{D}^p_{ij}}{\sqrt{\hat{D}^p_{kl}\hat{D}^p_{kl}}} \tag{33}$$

where c_p is a parameter controlling its evolution. The "delayed pointer" is initially assumed to be equal to the zero tensor, which is the case for well-annealed materials (Mánik et al., 2015). This is not necessarily true for our materials, but since the pre-straining in the present study is quite large, the "delayed pointer" at load reversal is similar to its true quantity and thus this is an appropriate simplification. The strain path change variables R_r and S_r are also assumed to be zero initially. It should be noted that the effect of orthogonal strain path changes, which is accounted for in the model by Mánik et al. (2015), has been neglected in the above equations as we are only simulating load reversal tests.

Finally, the loading/unloading conditions of plasticity are given in Kuhn-Tucker form as

$$\Phi \leq 0, \quad \dot{\lambda} \geq 0, \quad \dot{\lambda}\Phi = 0 \tag{34}$$

whereas the consistency condition, used to determine the plastic multiplier $\dot{\lambda}$ in the plastic domain, is expressed by

$$\dot{\lambda}\dot{\Phi} = 0 \tag{35}$$

The reader is referred to Mánik et al. (2015) for a more detailed description and interpretation of the constitutive relations accounting for the effects of strain path change.

5. Numerical simulations

5.1. Crystal plasticity and calibration of yield surfaces

In this section, the yield surface of the materials is calibrated using the crystal plasticity model described in Section 4.1. The parameters controlling the shape of the Yld2004-18p yield surface are typically determined from a large number of experimental tests (see, e.g., Fourmeau et al., 2011). It is, however, desirable to determine the behaviour of complex materials without performing extensive experimental testing. The anisotropy coefficients $\hat{c}'_{ij}$ and $\hat{c}''_{ij}$ will therefore be determined from virtual testing using polycrystal plasticity theory. In addition to the lower cost than experiments, virtual testing allows for performing tests in any direction and material plane, i.e., virtual testing is not restricted by experimental limitations.

Each material is represented by an RVE, see Figure 5, consisting of $10 \times 10 \times 10$ elements, where each element represents a grain. This results in a total of 1000 grains in the RVE of the polycrystalline material.

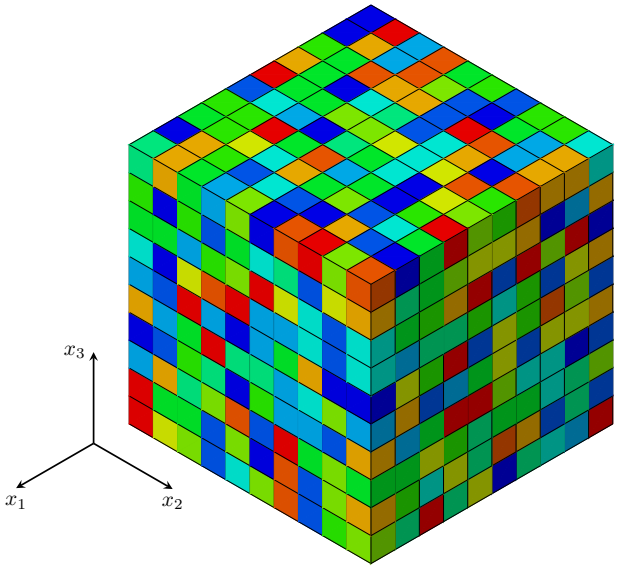

Figure 5: Representative volume element (RVE) of a polycrystal used in the calibration of the yield surfaces.

Periodic boundary conditions are applied to the nodes on the exterior boundaries to ensure periodicity. A convergence study was performed, where the number of elements per grain and the number of grains were varied. The details of that study are omitted here for brevity. It was found that this RVE contains a sufficiently large number of grains to predict the average stress state with adequate accuracy, and small enough to provide reasonable computational times. All elements/grains are given an initial orientation such that the ODF of the RVE is as close as possible to the ODF of the measured crystallographic texture for each alloy. The crystal orientations of the RVE are generated in the open source software DREAM.3D (Groeber and Jackson, 2014) by a stochastic iterative procedure.

The crystal plasticity model is implemented into a user material subroutine (VUMAT) for Abaqus/Explicit (Abaqus, 2014). An explicit integration scheme is utilized for time integration of the rate constitutive equations of single crystal plasticity (Zhang et al., 2014), along with explicit integration of the momentum equations. The grains are represented by linear eight-node elements with selective reduced integration (C3D8), i.e., reduced integration on the volumetric terms. The RVE is loaded with a strain rate of 10^{-3} s^{-1} in all simulations, and mass scaling is used to reduce the computational time. Throughout the simulations it is ensured that the response is quasi-static, i.e., that the kinetic energy is negligible.

Table 4: Crystal plasticity parameters governing elasticity, rate sensitivity and latent hardening.

$\hat{c}_{11}$ (MPa)	$\hat{c}_{12}$ (MPa)	$\hat{c}_{44}$ (MPa)	$\dot{\gamma}_0$ (s^{-1})	m	$q_{\alpha\beta}$
106 430	60 350	28 210	0.010	0.005	1.0 if $\alpha = \beta$ 1.4 if $\alpha \neq \beta$

Table 4 contains some of the crystal plasticity model parameters, which are common for a broad range of aluminium alloys from the literature (Khadyko et al., 2014, 2016b). These parameters are assumed constant for the materials at hand, while the parameters governing initial slip resistance and work hardening are dependent upon alloy and temper conditions. Note that a rather simple definition of the latent hardening matrix is used, with a single non-diagonal parameter. This choice could impact the response at large plastic deformations. In this paper, the crystal plasticity framework will only be used to determine the instance of initial yielding, i.e., to calibrate the yield surfaces. Thus, the current latent hardening matrix is deemed sufficiently accurate. The reader is referred to Khadyko et al. (2016a) for further details on latent hardening

and plastic anisotropy evolution.

We define a global Cartesian coordinate system (x_1, x_2, x_3) aligned with the principal axes of anisotropy of the extruded profile. The coordinate system is oriented so that ED is parallel to the x_1 axis, TD is parallel to the x_2 axis, and ND is parallel to the x_3 axis. In the following, all stress and strain quantities are related to this coordinate system.

Table 5: Crystal plasticity parameters governing initial slip resistance and work hardening.

Material	τ_0 (MPa)	$\theta_{\tau 1}$ (MPa)	τ_1 (MPa)	$\theta_{\tau 2}$ (MPa)	τ_2 (MPa)
AA6060-O	10.5	301.0	13.1	49.9	13.5
AA6060-T7	54.5	207.9	19.3	0.0	0.0
AA6060-T6	72.2	81.5	16.5	0.0	0.0
AA6082.25-O	20.4	236.9	13.5	25.7	15.7
AA6082.25-T7	58.3	190.1	18.7	0.0	0.0
AA6082.25-T6	107.1	30.4	200.0	5.5	200.0
AA6082.50-O	13.6	262.3	12.5	55.6	17.0
AA6082.50-T7	78.7	175.1	16.1	0.0	0.0
AA6082.50-T6	123.0	13.0	199.2	8.1	190.7

To include and study any effects of the strength and work hardening on the yield surfaces, the parameters controlling the slip resistance are fitted based on the experimental tests on smooth cylindrical specimens performed by Khadyko et al. (2014) and Khadyko (2018). The RVE is subjected to uniaxial tension along the x_2 axis (TD), i.e., the same direction as the experiments. The non-linear optimisation software LS-OPT (Stander et al., 2015) is used together with Abaqus to calibrate the parameters controlling the slip resistance using experimental data up to diffuse necking. In the optimisation procedure, Abaqus supplies the stress-strain curve from the RVE to LS-OPT which calculates the mean squared error between the numerical and experimental stress-strain curves. Based on the optimisation algorithm the slip resistance parameters are adjusted to minimise the mean squared error in the next iteration. Within each iteration, LS-OPT runs 10 simulations simultaneously with Abaqus varying these parameters. In general, after 15-20 iterations the mean squared error is reduced from 1-10 to approximately 10^{-5} and further iterations will not reduce the error. One of these simulations with the RVE is completed in approximately 50-60 min utilising 4 threads on an Intel Xeon X5690 CPU. Table 5 contains the optimised slip resistance parameters for the different materials, valid up to diffuse necking. For further details regarding calibration of slip resistance parameters, the reader is referred to Khadyko et al. (2015).

With all the parameters of the crystal plasticity model identified, the RVE can be used to determine the yield surfaces of the nine materials. Barlat et al. (2005) proposed a series of experimental and numerical tests to be performed in order to determine the anisotropy coefficients $\hat{c}'_{ij}$ and $\hat{c}''_{ij}$. These tests consist of uniaxial tension in seven different directions in the $x_1 - x_2$ plane, i.e., uniaxial tension in 15° increments from the x_1 axis to the x_2 axis, and balanced biaxial tension in the $x_1 - x_2$ plane. From these tests both the initial yield stress and the Lankford coefficients are used to calibrate the yield surface. In addition, the initial yield stress in simple shear in the $x_2 - x_3$ and $x_1 - x_3$ planes, and uniaxial tension tests oriented at 45° between the x_2 and x_3 axes, and between the x_1 and x_3 axes, are used. In order to perform tests at any angle from the principal axes of anisotropy of the material, the initial orientation of the RVE is rotated by an equal amount.

During the calibration process, it became clear that for some of the materials more tests were needed to get an accurate estimate of the yield surface. Particularly important were the plane-strain tension tests in the $x_1 - x_2$ plane at 0° and 90° from the x_1 axis. In addition, a plane-stress balanced biaxial strain test in the $x_1 - x_2$ plane was included, i.e., where the strain rates in the two in-plane directions are equal and greater than zero, i.e., $\dot{\varepsilon}_{11}/\dot{\varepsilon}_{22} = 1$. Note that this point coincides with that of balanced biaxial tension for an isotropic material. Also, five tests with different (negative) ratio between the strain rate along the x_1 and x_2 axes were included. These tests have the following strain-rate ratios: $\dot{\varepsilon}_{11}/\dot{\varepsilon}_{22} = -2.00, -1.57, -1.00,$

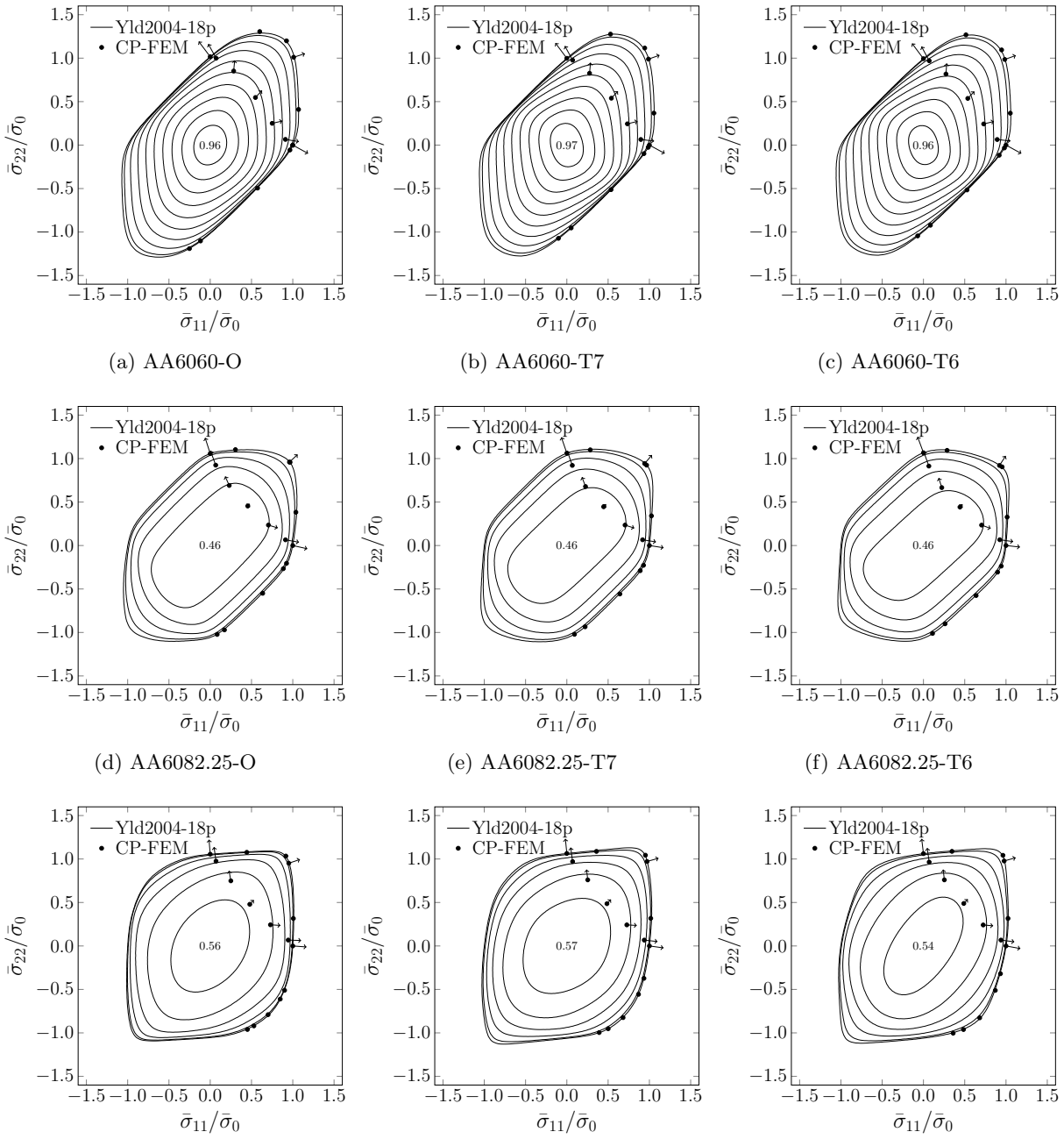

(a) AA6060-O (b) AA6060-T7 (c) AA6060-T6

(d) AA6082.25-O (e) AA6082.25-T7 (f) AA6082.25-T6

(g) AA6082.50-O (h) AA6082.50-T7 (i) AA6082.50-T6

Figure 6: Generated yield surfaces based on the CP-FEM, at a volume-average plastic work corresponding to 0.2% plastic strain along the reference direction, depicted in the $x_1 - x_2$ (ED-TD) plane. Contours of the normalised shear stress $\bar{\sigma}_{12}/\bar{\sigma}_0$ are plotted in 0.1 increments from zero, and the maximum value of $\bar{\sigma}_{12}/\bar{\sigma}_0$ is shown in the centre. Arrows represent the projections of the direction of plastic flow predicted by the CP-FEM.

-0.64 and -0.50.

For each test and for every material, the volume-average Cauchy stress tensor is extracted at a volume-average plastic work corresponding to 0.2% plastic strain for uniaxial tension along the x_1 axis, i.e., the reference direction. Further, the stress tensors for all the tests are normalised by the initial yield stress in

uniaxial tension along the reference direction, and the Lankford coefficient is found by taking the average value from 90% to 100% of the same value of plastic work.

The yield surface is calibrated as follows. The normalised volume-average Cauchy stress tensors and the Lankford coefficients are used in the evaluation of an error function, see Barlat et al. (2005). This error function is a function of the equivalent stress, Equation (20), which depends on the anisotropy coefficients $\hat{c}'_{ij}$ and $\hat{c}''_{ij}$ and the yield surface exponent a. Note that the yield surface shape is assumed invariant of pressure, thus $\phi = \varphi$ in Equation (19) during the calibration process. Further, the error function is minimised by varying these parameters with the global minimisation algorithm *basin-hopping* of the Scipy Python package (Scipy, 2017). The error function typically has several local minima, and therefore a global minimisation algorithm should be used. The generated yield surfaces for each material together with the predicted yield stresses by CP-FEM are depicted as projections in the $x_1 - x_2$ plane in Figure 6.

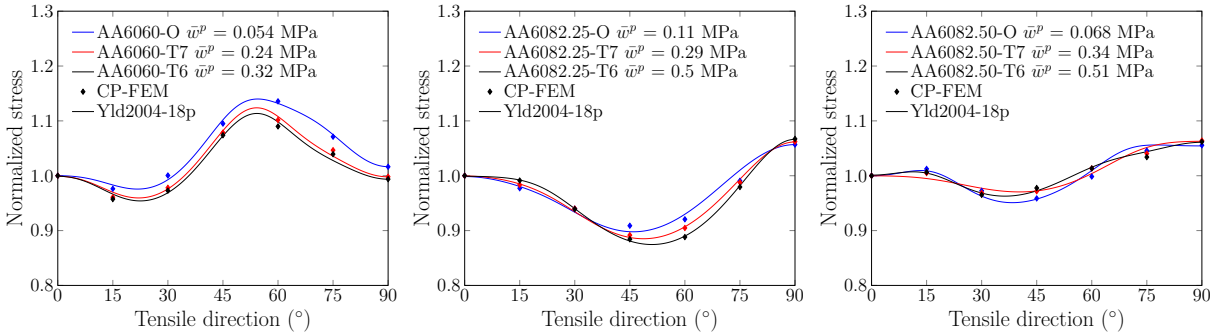

(a) AA6060 (b) AA6082.25 (c) AA6082.50

Figure 7: Normalised yield stress versus tensile direction in uniaxial tension, from the CP-FEM and the generated yield surfaces, at a volume-average plastic work corresponding to 0.2% plastic strain along the reference direction.

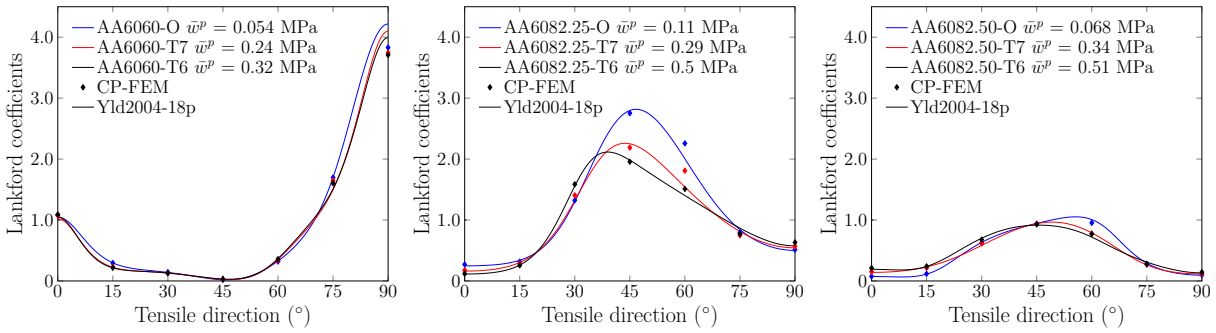

(a) AA6060 (b) AA6082.25 (c) AA6082.50

Figure 8: Lankford coefficients versus tensile direction for uniaxial tension, from the CP-FEM and the generated yield surfaces, at a volume-average plastic work corresponding to 0.2% plastic strain along the reference direction.

Although most of the stress points on the yield surface used in the calibration are located in the $x_1 - x_2$ plane, the yield surfaces are not biased with respect to this plane. As both the crystal plasticity model and the Yld2004-18p yield function depend only on the deviatoric stress state, these points are equivalent to other points on the yield surface, e.g., uniaxial tension along the x_1 axis is equivalent to balanced biaxial tension/compression in the $x_2 - x_3$ plane. The strength differential effect is not accounted for by including non-Schmid effects in the crystal plasticity model, and does not affect the calibration of the yield surfaces.

Figure 6 shows the differences between the yield surfaces and it is clear that while the yield surfaces are similar for the tempers of the same alloy, the difference between the alloys is considerable due to the crystallographic texture. The largest difference between tempers for the same alloy is seen for the AA6082.50

alloy as the contours of increasing normalised shear stress are different. This is also the alloy where the difference in maximum shear stress is the greatest between tempers.

Table 6: Calibrated anisotropy coefficients and yield surface exponent for the Yld2004-18p yield criterion.

Material		AA6060			AA6082.25			AA6082.50	
Temper	O	T7	T6	O	T7	T6	O	T7	T6
a	9.2	11.4	11.8	18.9	13.6	13.5	17.0	14.5	12.5
$\hat{c}'_{12}$	1.0000	1.0000	1.0000	1.0000	1.0000	1.0000	1.0000	1.0000	1.0000
$\hat{c}'_{13}$	1.0000	1.0000	1.0000	1.0000	1.0000	1.0000	1.0000	1.0000	1.0000
$\hat{c}'_{21}$	−0.7261	0.2604	−2.2769	0.6684	0.6898	0.6441	−0.3166	−3.3119	0.9218
$\hat{c}'_{23}$	0.1009	0.4756	−0.4709	1.1443	1.0272	1.0412	2.5260	−1.0938	0.6785
$\hat{c}'_{31}$	−0.1925	−2.2405	0.2555	0.5263	0.6059	0.6559	−0.5265	−3.6098	−0.5508
c'_{32}	−0.0950	−0.1944	0.2118	0.8230	0.8885	0.8653	−0.5163	−1.0424	0.8985
c'_{44}	−0.9592	0.1896	−0.1895	−1.0469	1.0120	0.9258	0.9885	1.0803	1.0859
c'_{55}	−1.2663	−0.1630	−0.1674	−1.0803	1.1697	1.4981	0.7676	−0.8979	0.8500
$\hat{c}'_{66}$	−0.9536	1.0997	−1.0957	0.8995	0.9321	0.9452	1.1178	−0.6982	−0.8305
$\hat{c}''_{12}$	−0.0641	0.8676	1.1498	1.0868	0.7564	0.6093	1.1378	1.8762	0.4348
$\hat{c}''_{13}$	−1.0887	2.2273	−0.2049	1.4677	1.1787	0.9544	2.6320	1.5935	−0.0688
$\hat{c}''_{21}$	−1.3105	−0.5072	−1.5280	0.7687	0.8525	0.8362	0.3832	−2.3255	−0.3157
$\hat{c}''_{23}$	−1.5205	1.7280	−1.7423	1.1013	1.0114	1.0750	1.2385	0.2799	1.0286
$\hat{c}''_{31}$	−1.2515	−1.2435	−0.7779	0.9502	1.1155	1.1397	−1.9285	−3.0594	1.1692
$\hat{c}''_{32}$	1.0219	0.6461	−0.6487	0.6869	0.9250	0.9613	−0.5312	−0.8772	1.2030
$\hat{c}''_{44}$	0.1129	0.8948	0.9069	1.1840	1.2775	1.3740	0.8826	0.7526	0.8661
$\hat{c}''_{55}$	0.0064	1.2337	1.2410	1.0164	1.0073	0.7300	−0.8001	−0.6629	−0.6963
$\hat{c}''_{66}$	−0.3154	−0.1672	−0.1838	1.1146	1.1609	1.2299	0.4342	0.8519	0.7349

Figure 7 and Figure 8 compare in turn the normalised yield stresses and Lankford coefficients as functions of the tensile direction, in the $x_1 - x_2$ plane, for the different materials. The differences between tempers of the same alloy are seen more clearly in these figures, although the main trends are similar for the same alloy. The corresponding Yld2004-18p yield surface parameters are given in Table 6.

The main source of anisotropy is assumed to be the crystallographic texture (Engler and Randle, 2009). In the present study, effects of other microstructural features, such as the size and shape of grains and the precipitate structure, are thus neglected. We note that the calibrated yield surfaces are initial yield surfaces, and during extensive plastic deformation the texture and the anisotropy of the materials will evolve. The result is that the yield surface shape evolves accordingly and the initial yield surface deviates from the current yield surface of the material.

5.2. Phenomenological plasticity and work-hardening behaviour

The strength differential effect is described by the pressure-dependent yield criterion defined in Equation (19), where the pressure sensitivity is controlled by the parameter α. The values of α for the current materials are obtained from the experimental data and results presented in Holmen et al. (2017). These values are compiled in Table 7. The reader is referred to Holmen et al. (2017) for details on the parameter identification.

The remaining model parameters govern isotropic and kinematic hardening, work-hardening stagnation and permanent softening, are calibrated in a two step procedure. It is useful to express the parameters of the isotropic and kinematic hardening rules as

$$\theta_{Ri} = \kappa_i \theta_i, \quad \theta_{\chi i} = (1 - \kappa_i)\theta_i \tag{36}$$

Table 7: Pressure sensitivity parameter. From Holmen et al. (2017).

Material	β (°)	$\alpha = \frac{1}{3}\tan\beta$
AA6060-O	0.7	0.004
AA6060-T7	1.7	0.010
AA6060-T6	2.2	0.013
AA6082.25-O	1.2	0.007
AA6082.25-T7	2.2	0.013
AA6082.25-T6	3.5	0.020
AA6082.50-O	0.9	0.005
AA6082.50-T7	2.5	0.015
AA6082.50-T6	3.6	0.021

$$Q_{Ri} = \kappa_i Q_i, \quad Q_{\chi i} = (1 - \kappa_i) Q_i \tag{37}$$

where there is no sum on i and it is assumed that the number of isotropic and kinematic hardening terms is the same, i.e., $N_V = N_\chi$. A three-term hardening rule is adopted so that $N_V = N_\chi = 3$. The parameters Q_i and θ_i define the work hardening of the material under monotonic loading, whereas κ_i define the partitioning into isotropic and kinematic hardening of the different hardening terms. This partitioning is possible because the isotropic and kinematic hardening rules give identical results in monotonic uniaxial tension.

In the first step, it is assumed that the work hardening is fully isotropic, i.e., all κ_i are equal to unity, and the parameters Q_i and θ_i are identified using the stress-strain curves from monotonic tensile tests on smooth cylindrical specimens performed by Khadyko et al. (2014) and Khadyko (2018). In the second step, the stress-strain curves from the reversed loading tests subjected to 10% and 40% pre-compression (10% and 30% for the AA6060 alloy in temper O) are used to partition the work hardening into isotropic and kinematic contributions and to determine the parameters controlling work-hardening stagnation and permanent softening.

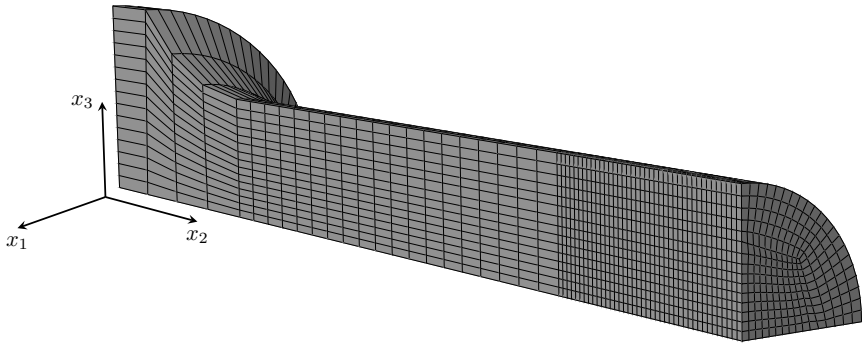

Figure 9: Finite element mesh of the smooth cylindrical tensile specimen, with tensile axis along the x_2 axis (TD).

To determine the parameters Q_i and θ_i, the smooth cylindrical tensile specimen used by Khadyko et al. (2014) is modelled in Abaqus/Standard. The phenomenological plasticity model described in Section 4.2 is implemented into a user material subroutine (UMAT) for Abaqus/Standard. A semi-implicit backward-Euler integration scheme is used to update the stress state for plastic loading steps. To ensure sufficient accuracy of the integration point values, substepping is employed (Dæhli et al., 2017). Isotropic elasticity is assumed with Young's modulus of $E = 70000$ MPa and Poisson's ratio of $\nu = 0.3$. The plasticity model is used in simulations with the calibrated pressure-sensitive anisotropic yield surface and isotropic hardening. The finite element mesh of the smooth tensile specimen is shown in Figure 9, with its tensile axis along the

x_2 axis (TD). Due to the orthotropic symmetry, only one-eighth of the specimen is modelled to reduce the computation time. Linear eight-node elements with selective reduced integration (C3D8) are used, where the dimension of the centre-most element is $0.15 \times 0.15 \times 0.15$ mm^3. Extensive testing with different element sizes showed that the selected mesh is appropriate for determining the hardening behaviour of the materials. The FE model in Abaqus is coupled to the non-linear optimisation software LS-OPT in the calibration procedure. The initial yield stress σ_0 is found from the crystal plasticity model for uniaxial tension along the reference direction, i.e., the x_1 axis (ED). The parameters Q_i and θ_i, $(i = 1, 2, 3)$, are calibrated by minimising the mean squared error between the stress-strain curves to failure from the FE simulation and the experimental tests. The resulting initial yield stress and hardening parameters are given in Table 8. Note that the presence of voids is not accounted for during the calibration of the phenomenological plasticity model, and thus the work hardening of the materials is probably underestimated at large strains.

Table 8: Initial yield stress and parameters of the three-term hardening rule.

Material	σ_0 (MPa)	θ_1 (MPa)	Q_1 (MPa)	θ_2 (MPa)	Q_2 (MPa)	θ_3 (MPa)	Q_3 (MPa)
AA6060-O	27.6	1844.8	34.7	400.5	28.8	83.5	91.5
AA6060-T7	124.6	1182.8	27.7	1094.8	28.1	39.6	726.9
AA6060-T6	170.8	549.2	19.9	476.3	17.8	70.0	124.9
AA6082.25-O	57.6	2661.3	44.6	382.2	32.6	120.8	91.0
AA6082.25-T7	163.6	1300.1	28.9	1301.2	40.7	52.3	232.9
AA6082.25-T6	299.5	470.5	28.5	485.0	29.8	50.0	279.4
AA6082.50-O	37.1	2009.9	39.3	233.6	30.9	208.2	69.5
AA6082.50-T7	189.9	1000.0	20.0	1366.5	41.1	29.3	153.5
AA6082.50-T6	284.1	8231.8	20.7	320.4	32.5	300.9	33.6

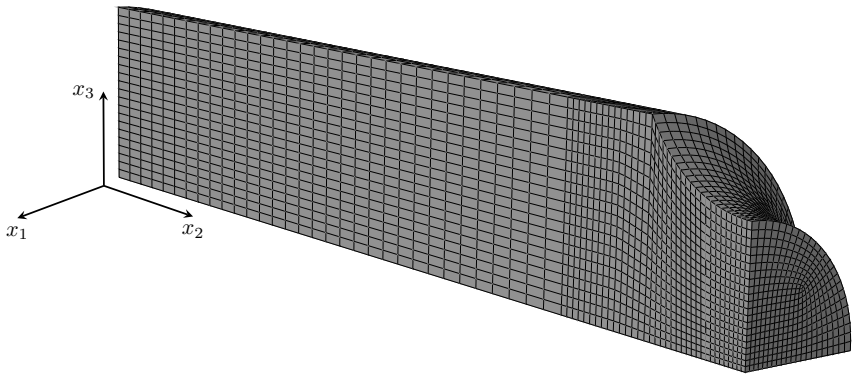

Figure 10: Finite element mesh of the diabolo-shaped specimen, with tensile axis along the x_2 axis (TD).

To determine the partitioning into isotropic and kinematic hardening and the parameters controlling work-hardening stagnation and permanent softening, the reversed loading tests subjected to 10% and 40% pre-compression are simulated. Figure 10 shows the FE mesh of the diabolo-shaped specimen, and again only one-eighth of the specimen is modelled to reduce computational time. Symmetry boundary conditions are applied, and at the end of the specimen, boundary conditions to replicate conditions at the threaded section are enforced. Linear eight-node elements with selective-reduced integration (C3D8) are used in Abaqus/Standard, where the dimension of the centre-most element is $0.12 \times 0.12 \times 0.12$ mm^3. As before, the FE model is coupled to LS-OPT in the calibration procedure, and the mean squared error between the stress-strain curves of the FE simulation and the experimental tests is minimised by varying the relevant parameters: $\kappa_1, \kappa_2, \kappa_3$, c_p, k_r, c_r and q_r. The resulting parameters are given in Table 9 and Table 10.

Table 9: Parameters controlling the partitioning into isotropic and kinematic hardening.

Material	κ_1	κ_2	κ_3
AA6060-O	1.0000	0.4368	1.0000
AA6060-T7	0.3589	0.5986	1.0000
AA6060-T6	0.4751	0.8193	1.0000
AA6082.25-O	0.9304	0.2284	1.0000
AA6082.25-T7	0.6430	0.0000	1.0000
AA6082.25-T6	0.0000	0.0000	1.0000
AA6082.50-O	0.9418	0.0000	1.0000
AA6082.50-T7	0.4847	0.0000	1.0000
AA6082.50-T6	0.0000	0.3269	1.0000

Table 10: Parameters governing work-hardening stagnation and permanent softening.

Material	c_p	k_r (MPa)	c_r	q_r
AA6060-O	26.1	2164.8	12.3	2.82
AA6060-T7	13.9	1953.8	0.0	0.00
AA6060-T6	10.5	1441.5	0.0	0.00
AA6082.25-O	11.6	1127.3	32.4	0.27
AA6082.25-T7	7.1	1025.2	28.8	0.02
AA6082.25-T6	19.2	2688.1	6.9	2.90
AA6082.50-O	13.7	1262.1	24.9	0.72
AA6082.50-T7	7.2	1500.7	0.0	0.00
AA6082.50-T6	13.2	1414.1	0.0	0.00

5.3. Loading histories from the reversed loading tests

The FE model of the diabolo-shaped specimen in Figure 10 is now subjected to the same load histories as applied in the reversed loading tests, using the phenomenological plasticity model with the calibrated parameter set. As before, the simulations are performed in Abaqus/Standard. Figure 11 presents the stress-strain curves from the finite element simulations together with the experiments. Generally good agreement is observed between the experimental and numerical curves, and especially good agreement is found for the AA6082.25 alloy. For the two other alloys, small discrepancies are observed as the stress level in compression and in monotonic tension is slightly higher in magnitude in the simulations than in the experiments, except for the AA6060 alloy in temper O.

The deviations may come from inaccuracies in the calibrated yield surfaces, or the fact that the phenomenological model does not account for the evolution of the yield surface. During plastic deformation the crystallographic texture of the materials will evolve and affect the yield surface of the material and the plastic response of the specimen. From Figure 4, it was observed that the AA6060 alloy developed a diamond-shaped fracture surface, which the phenomenological model is not fully able to recreate. This will yield inaccuracies, since the logarithmic strain measure is based on an elliptical cross-section area, as explained in Section 3.1. A discussion of this source of error is provided in Frodal et al. (2017). In addition, the strain path change model is not fully able to recreate the work-hardening stagnation observed for the alloys in temper O, as the experimental curves show that this transient appears to decrease for larger pre-compression levels. Also after the transient phase the resumed work-hardening rate deviates from that of the experiments for the alloys in temper O. This may be caused by the incorrectly described work-hardening stagnation behaviour as it would lead to an earlier localisation of deformation in the centre of the notch area. For the AA6082.50 alloy in temper T7, the permanent softening is overestimated for 10, 20 and 30% pre-compression, whereas it is well predicted for the 40% pre-compression curves used in the calibration process.

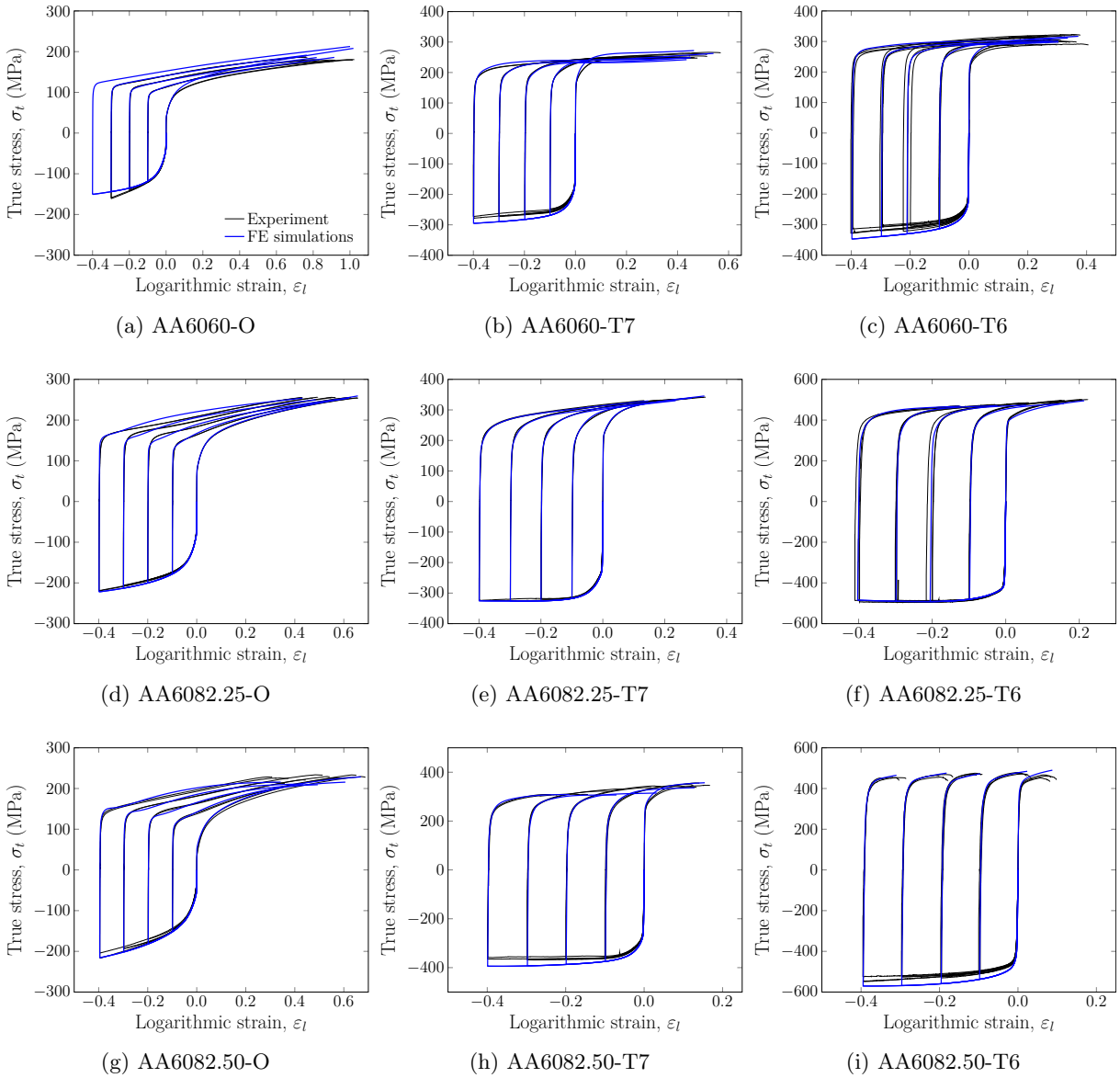

(a) AA6060-O (b) AA6060-T7 (c) AA6060-T6

(d) AA6082.25-O (e) AA6082.25-T7 (f) AA6082.25-T6

(g) AA6082.50-O (h) AA6082.50-T7 (i) AA6082.50-T6

Figure 11: Stress-strain curves for the three alloys in different tempers, from experiments (black curves) and finite element simulations (blue curves), until failure in the experiment.

Figure 12 shows the stress-strain curves for the AA6082.25 alloy in T7 temper, including finite element simulations with different hardening models. Here the importance of the strain path change model is revealed. It is seen that the simulations with either isotropic hardening or combined isotropic and kinematic hardening do not capture the permanently reduced stress level in tension after load reversal. In contrast, the full model, involving all the parameters calibrated above, represents the stress level and the response of the specimen accurately, which is important when investigating failure.

The Lankford coefficients calculated from the finite element simulations are compiled in Table 11. Comparing the coefficients with the experimental values in Table 3, it is found that the coefficients for all tempers of the AA6082.25 alloy are in good agreement with the experimental values. For the two other alloys, the simulated Lankford coefficients typically overestimate the plastic anisotropy, with the exception of the AA6060 alloy in temper O and the AA6082.50 alloy in temper T6. Further, the numerical model

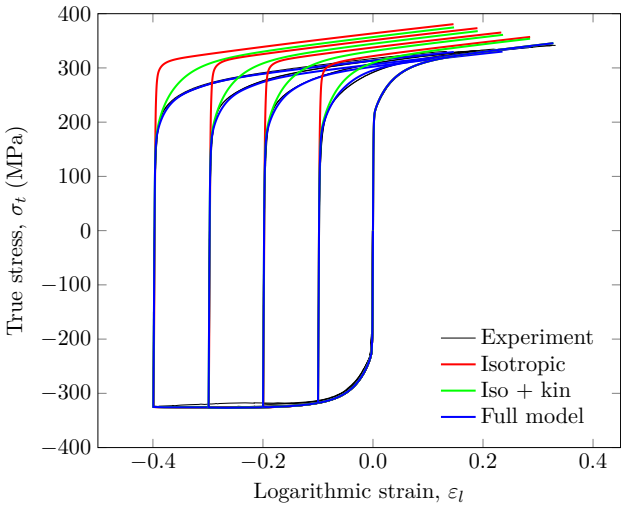

Figure 12: Stress-strain curves for the AA6082.25 alloy in T7 temper, from experiments and finite element simulations with different hardening models. Note that the experimental (black) curves lie under the (blue) curves for the full model.

does not capture the evolution of the Lankford coefficients, with increasing pre-compression as seen in the experiments. This indicates that the yield surface evolves with plastic deformation, affecting the response of the specimen.

Table 11: Calculated Lankford coefficients in tension, compression and in tension after pre-compression from the finite element model of the reversed loading tests.

Material	Tension	Compression	In tension after 10% pre-compression	In tension after 20% pre-compression	In tension after 30% pre-compression	In tension after 40% pre-compression
AA6060-O	1.04	0.96	0.93	0.92	0.90	0.94
AA6060-T7	1.67	1.59	1.52	1.48	1.50	1.54
AA6060-T6	1.62	1.59	1.49	1.43	1.43	1.43
AA6082.25-O	0.78	0.76	0.81	0.82	0.81	0.81
AA6082.25-T7	0.91	0.89	0.92	0.93	0.94	0.94
AA6082.25-T6	1.00	1.00	0.99	1.00	1.00	0.99
AA6082.50-O	0.25	0.26	0.30	0.33	0.35	0.38
AA6082.50-T7	0.30	0.29	0.35	0.41	0.44	0.44
AA6082.50-T6	0.52	0.49	0.55	0.57	0.61	0.62

The loading and deformation histories are then extracted from the critical element in the full model, i.e., the element where fracture is assumed to initiate. The critical element is assumed to be located in the centre of the specimen where the stress triaxiality is the highest at material failure. Due to the orthotropic material symmetry, the stress state of this element is already in the principal stress space. Following Dæhli et al. (2017), we can write the normal stress components on vector form as

$$\begin{bmatrix} \Sigma_{11} \\ \Sigma_{22} \\ \Sigma_{33} \end{bmatrix} = \Sigma_{eq}^{vm} \left[\frac{2}{3} \begin{pmatrix} \cos\theta_L \\ \cos(\theta_L - \frac{2\pi}{3}) \\ \cos(\theta_L + \frac{2\pi}{3}) \end{pmatrix} + T \begin{pmatrix} 1 \\ 1 \\ 1 \end{pmatrix} \right] \tag{38}$$

where Σ_{eq}^{vm} is the equivalent von Mises stress, θ_L is the deviatoric angle, and T is the stress triaxiality defined as

$$T = \frac{\Sigma_{kk}}{3\Sigma_{eq}^{vm}} \tag{39}$$

Note that capital letters are now used for stress related quantities to emphasise that they are the macroscopic quantities of the unit cell model in Section 5.4.

The ratios between the principal stress components are uniquely defined by the stress triaxiality ratio and the deviatoric angle. Thus, the non-proportional loading path that will be enforced on the unit cell model is uniquely defined by the stress triaxiality ratio and the deviatoric angle as functions of the accumulated von Mises strain, which is given by

$$E_{acc}^{vm} = \int_0^t \sqrt{\frac{2}{3} D'_{ij} D'_{ij}} dt \tag{40}$$

where D'_{ij} is the deviatoric part of the rate of deformation tensor.

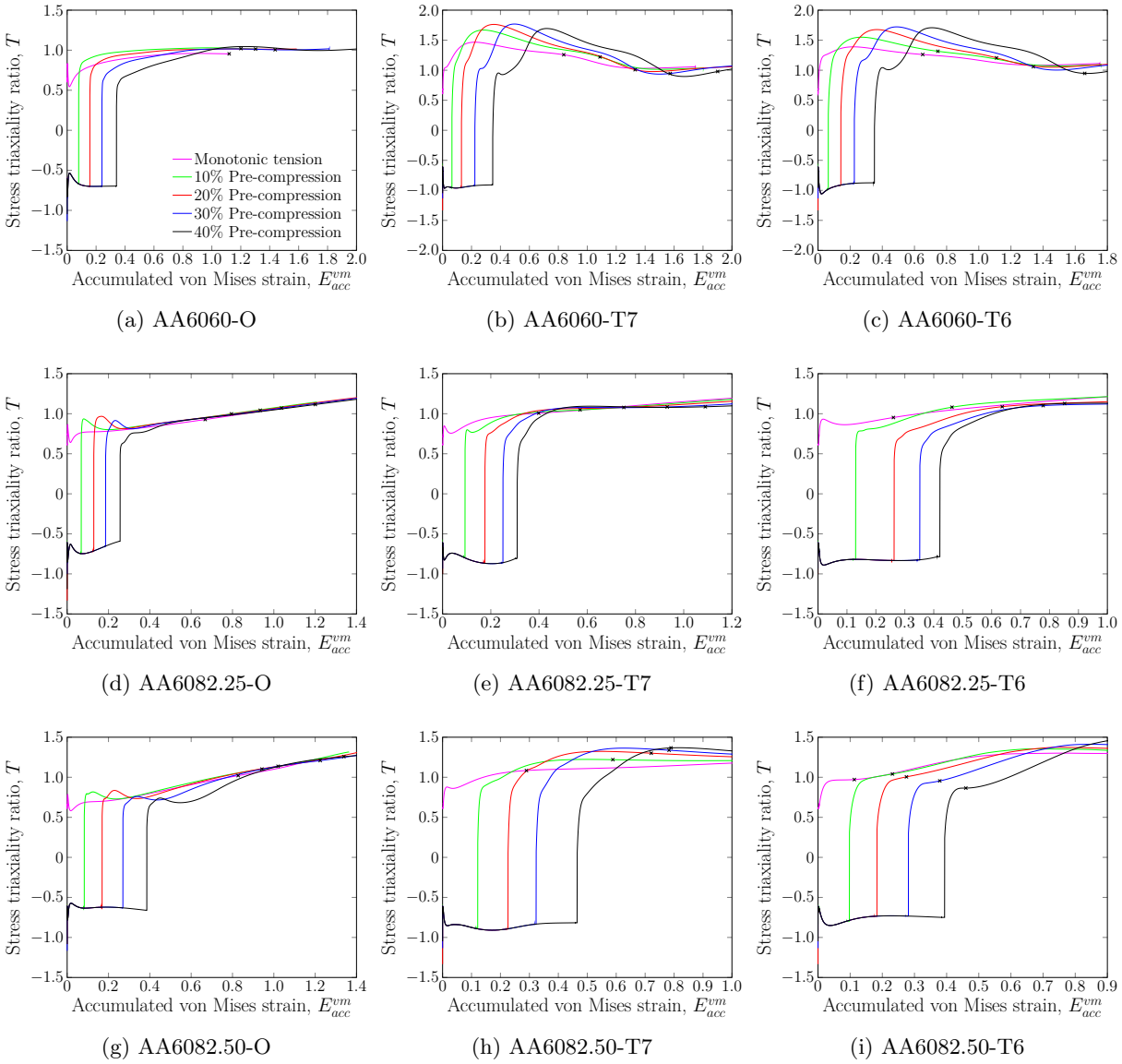

(a) AA6060-O (b) AA6060-T7 (c) AA6060-T6

(d) AA6082.25-O (e) AA6082.25-T7 (f) AA6082.25-T6

(g) AA6082.50-O (h) AA6082.50-T7 (i) AA6082.50-T6

Figure 13: Stress triaxiality ratio versus accumulated von Mises strain in the centre element from the reversed loading tests. The point corresponding to failure in the experiments is indicated with a cross.

The stress triaxiality ratio and the deviatoric angle as functions of the accumulated von Mises strain from the critical element are shown in Figure 13 and Figure 14, respectively. The point corresponding to

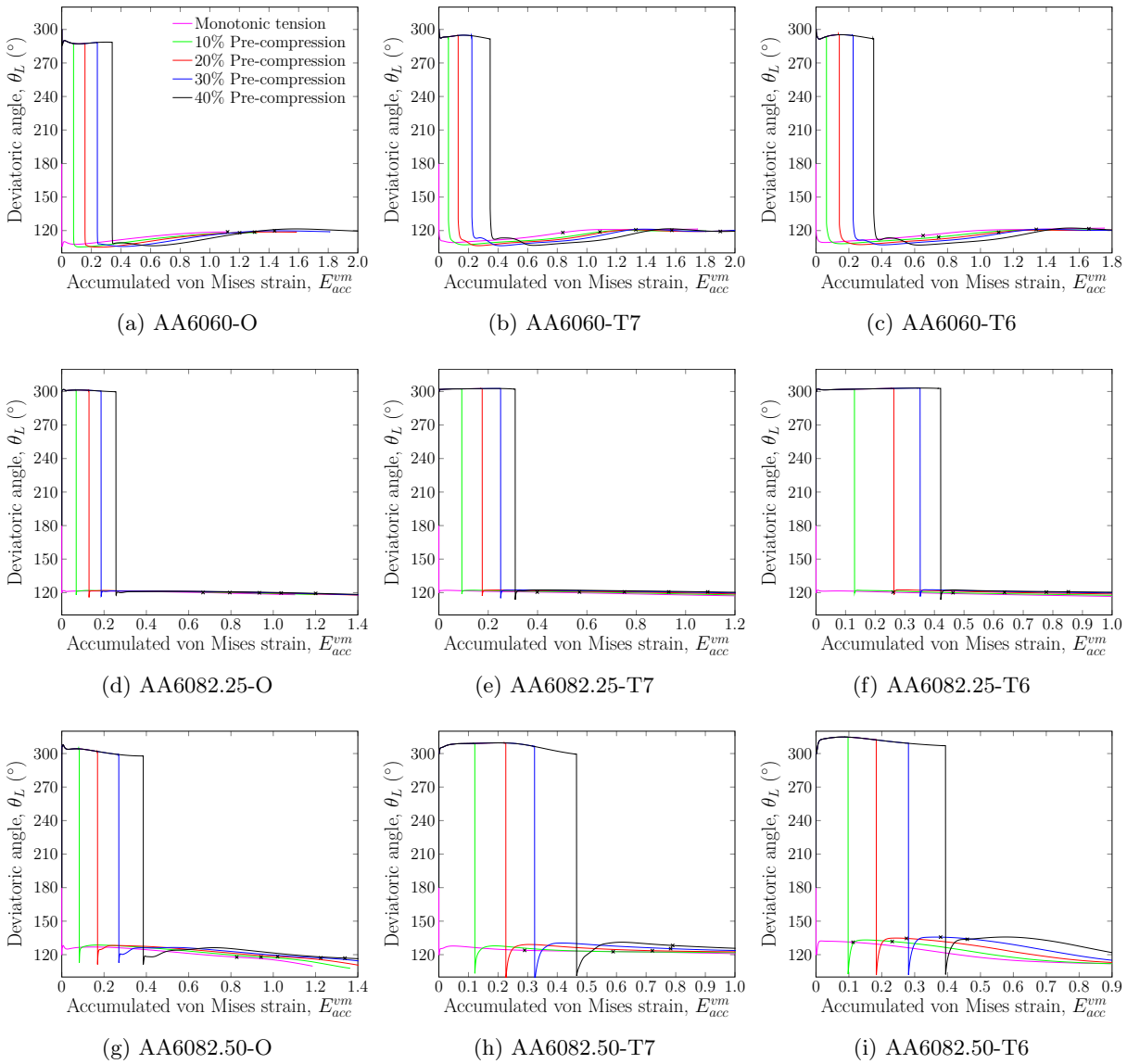

(a) AA6060-O (b) AA6060-T7 (c) AA6060-T6

(d) AA6082.25-O (e) AA6082.25-T7 (f) AA6082.25-T6

(g) AA6082.50-O (h) AA6082.50-T7 (i) AA6082.50-T6

Figure 14: Deviatoric angle versus accumulated von Mises strain in the centre element from the reversed loading tests. The point corresponding to failure in the experiments is indicated with a cross.

failure in the experiments is indicated with a cross. The plastic anisotropy, strength and work hardening of the materials are seen to have a great impact on the evolution of the triaxiality and the deviatoric angle, and are thus assumed also to affect the ductile failure. Also, the evolution after pre-compression is distinct from monotonic tension for a given material. The curves are different for each pre-compression level, caused by the change in specimen geometry and work hardening of the material. The reader should note here that a deviatoric angle of 300° and 120°, corresponds to a Lode parameter of +1 and −1, respectively.

5.4. Unit cell modelling

To investigate possible fracture mechanisms involved during the reversed loading tests, unit cell simulations are conducted. The non-proportional loading paths extracted from the critical element in Section 5.3 are enforced on the unit cell. The unit cell is modelled with a rigid particle in the centre and a matrix material governed by the phenomenological plasticity model given in Section 4.2.

The material region defined by the critical element in Section 5.3 is now represented by the unit cell model, see Figure 15a. Due to the orthotropic symmetry of the material and the stress and strain state of the material region, i.e., the orthotropic symmetry axes coincide with the principal directions of stress and strain, only one-eighth of the unit cell is modelled to reduce computational time. Figure 15b shows the FE mesh of the unit cell model used for the AA6082.50 alloy in temper O, with approximately 15 000 elements. The particle is modelled as an analytical rigid part in Abaqus/Standard, and is excluded from the figure since it has no mesh. The FE model consists of 5000 to 18 000 linear eight-node elements with selective-reduced integration (C3D8), where the number of elements used depends on the plastic anisotropy and ductility of the material at hand. A thorough mesh convergence study was conducted for each material, but these details are omitted here for brevity.

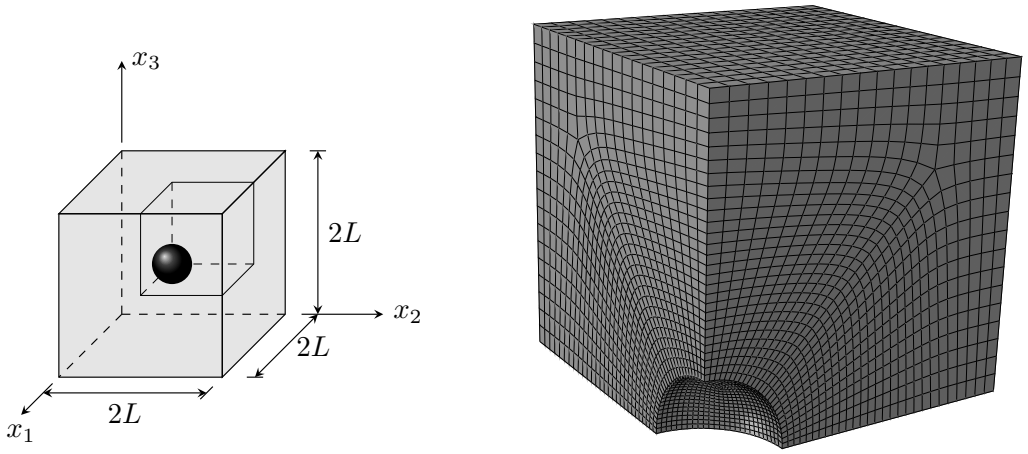

Figure 15: (a) The unit cell model with dimensions $2L \times 2L \times 2L$, and (b) the finite element mesh of the one-eighth model, for the AA6082.50 alloy in temper O.

The dimensions of the unit cell are taken to be equal along the orthotropic symmetry axes, i.e., $L_1 = L_2 = L_3 = 2L$, where L is the length of the one-eighth model, Figure 15b. The rigid particle in the centre is spherical, i.e., $R_1 = R_2 = R_3 = R$, with no cohesion to the matrix material. Hence, the unit cell model represents a uniform distribution of equally spaced, pre-nucleated voids with equally sized spherical particles inside, where we neglect any effects of initial void/particle shape, spatial distribution and debonding.

Periodicity is ensured by enforcing the exterior boundaries of the unit cell model to remain straight during deformation. A friction-less surface to surface contact formulation is used for the contact between the void surface and the analytical rigid particle. To impose the non-proportional loading history to the unit cell, non-linear kinematic constraints are used. Following Dæhli et al. (2016b, 2017), based on the work of Faleskog et al. (1998) and Kim et al. (2004) who introduced a technique for proportional loading of the unit cell, the principal stress ratios are introduced as

$$\psi_1 = \frac{\Sigma_{11}}{\Sigma_{\max}}, \quad \psi_2 = \frac{\Sigma_{22}}{\Sigma_{\max}}, \quad \psi_3 = \frac{\Sigma_{33}}{\Sigma_{\max}} \tag{41}$$

where $\Sigma_{\max} = \max(\Sigma_{11}, \Sigma_{22}, \Sigma_{33})$. Hence, by Equation (38), the principal stress ratios are uniquely defined by the stress triaxiality ratio and the deviatoric angle as functions of the accumulated von Mises strain, see Figure 13 and Figure 14.

The multi-point constraint (MPC) subroutine in Abaqus/Standard is used to impose the non-linear kinematic constraints to the unit cell model. The MPC subroutine is supplied with the principal stress ratios that are updated incrementally with the accumulated von Mises strain to enforce the non-proportional loading path to the unit cell model. For further details regarding the non-linear kinematic constraints, the

reader is referred to Faleskog et al. (1998); Kim et al. (2004); Barsoum and Faleskog (2007); Cheng and Guo (2007); Vadillo and Fernández-Sáez (2009); Wong and Guo (2015); Liu et al. (2016) and Dæhli et al. (2017).

The initial void/particle volume fraction of the unit cell model is given by

$$f_0 = \frac{V_{v,0}}{V_{uc,0}} = \frac{\pi R^3}{6L^3} \tag{42}$$

where $V_{v,0}$ and $V_{uc,0}$ are the initial volume of the void/particle and the unit cell model, respectively. For each material f_0 is calibrated to the monotonic tension test on the diabolo-shaped specimen. Thus, f_0 is adjusted such that the point of coalescence in the unit cell model corresponds to the point of failure in the experimental tests under monotonic tension. This is achieved by making sure that the accumulated von Mises strains in the unit cell model at coalescence and the critical element at failure are equal. In the current work, we define coalescence as the point where the deformation mode of the unit cell model becomes uniaxial (Koplik and Needleman, 1988).

The calibrated value of f_0 will here be bounded from above by the measured particle fractions of the materials. The measured fractions of primary particles are $f_p = 0.0093$, $f_p = 0.0120$ and $f_p = 0.0139$ for the AA6060, AA6082.25 and AA6082.50 alloys, respectively (Frodal et al., 2017). The calibrated values of f_0 are given in Table 12.

Table 12: Initial void/particle volume fractions.

Material	f_0
AA6060-O	0.0015
AA6060-T7	0.0006
AA6060-T6	0.0022
AA6082.25-O	0.0025
AA6082.25-T7	0.0075
AA6082.25-T6	0.0120
AA6082.50-O	0.0078
AA6082.50-T7	0.0139
AA6082.50-T6	0.0139

For the AA6082.25 in T6 temper and the AA6082.50 alloy in T7 and T6 temper, f_0 is restricted by the measured particle fraction. In order for these materials to have coalescence of the unit cell corresponding to failure in the experiments subjected to monotonic tension, the calibrated values of f_0 were 0.0320, 0.0265 and 0.1000 for the AA6082.25 alloy in T6 temper and the AA6082.50 alloy in T7 and T6 tempers, respectively. These high values of f_0 indicate that other failure mechanisms and effects than those included in the unit cell model are present, e.g., effects of the large grain size for the AA6082.50 alloy, which reduce the material ductility (Frodal et al., 2017). Thus, for these materials the point of coalescence in the unit cell model will not coincide with failure in the experiments subjected to monotonic tension.

For the other materials, a lower value of f_0 than the measured particle fraction was found from the calibration, indicating that only a portion of the particles nucleate voids. By examining Table 8 and Table 12 it is apparent that f_0 varies with the strength of the material, i.e., a higher strength typically yields a higher value of f_0. It is reasonable to assume that this is linked to a higher void nucleation rate when the stress level is increased. For the AA6060 alloy, the calibrated value of f_0 is greater for temper O than for temper T7 even though the latter has the higher strength. This is likely related to the significant differences observed in the stress triaxiality level, Figure 13, the deviatoric angle, Figure 14, and the work hardening of the different tempers for this alloy. Note that care should be taken when interpreting the results and microstructural input of the unit cell model, as this model represents complex materials in an idealised way.

5.5. Unit cell results

The unit cell model is now subjected to all the non-proportional loading paths given in Figure 13 and Figure 14, i.e., all pre-deformation levels for all the materials. Figure 16 shows the response of the unit cell model in terms of the normalised von Mises stress versus the accumulated von Mises strain. The stress-strain curves obtained with the unit cell model are markedly different for the various alloy-temper combinations. However, the stress-strain curves for the three materials in O temper are similar. These materials have the greatest hardening and exhibit work-hardening stagnation after pre-compression.

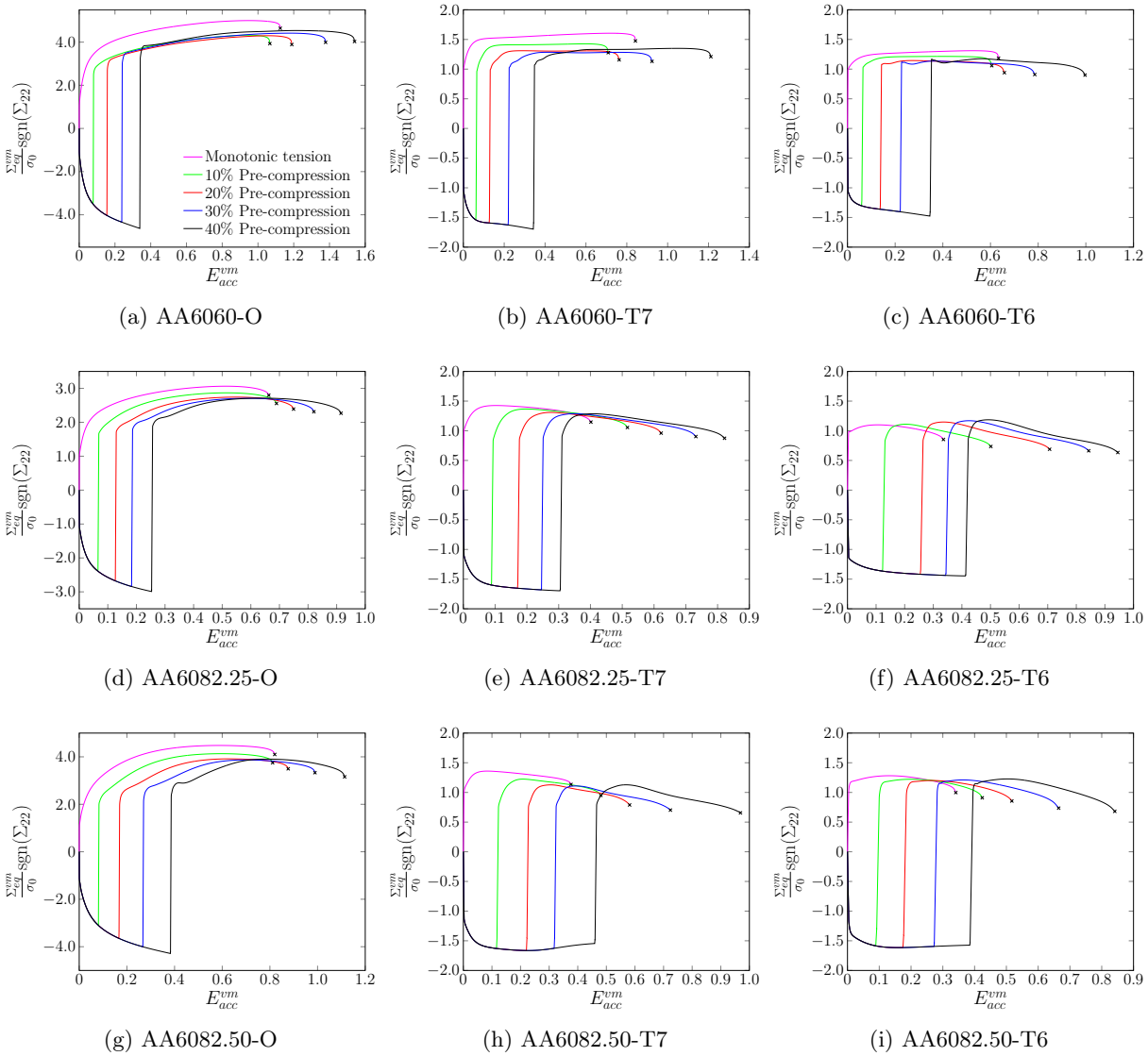

(a) AA6060-O (b) AA6060-T7 (c) AA6060-T6

(d) AA6082.25-O (e) AA6082.25-T7 (f) AA6082.25-T6

(g) AA6082.50-O (h) AA6082.50-T7 (i) AA6082.50-T6

Figure 16: Macroscopic stress-strain curves in terms of normalized von Mises stress and accumulated von Mises strain for the unit cell model. The point corresponding to coalescence is indicated with a cross.

For some of the materials, the stress level after pre-compression is lower than for monotonic tension, as clearly seen for the AA6060 alloy in T7 temper, due to the permanent softening of the material after load reversal. A softening effect is also observed in compression after approximately 20% pre-deformation for the AA6082.50 alloy in temper T7 and T6. This is caused by the low work hardening in combination with the shape of the yield surface for these materials, as the von Mises stress curves from the critical element of the

diabolo-shaped specimen also exhibit the same trend. Thus, this is an effect of the metal plasticity as the stress state moves in stress space along the yield surface of the material.

Figure 17 shows plots of the initial configuration and the configuration at the onset of void coalescence for the AA6082.25 alloy in temper O. Comparing the deformed configuration at the onset of coalescence after monotonic tension and after 40% pre-compression, it is apparent that the local matrix accumulated plastic strains are higher after pre-compression. Also the shape and size of the void are different after 40% pre-compression compared to monotonic tension.

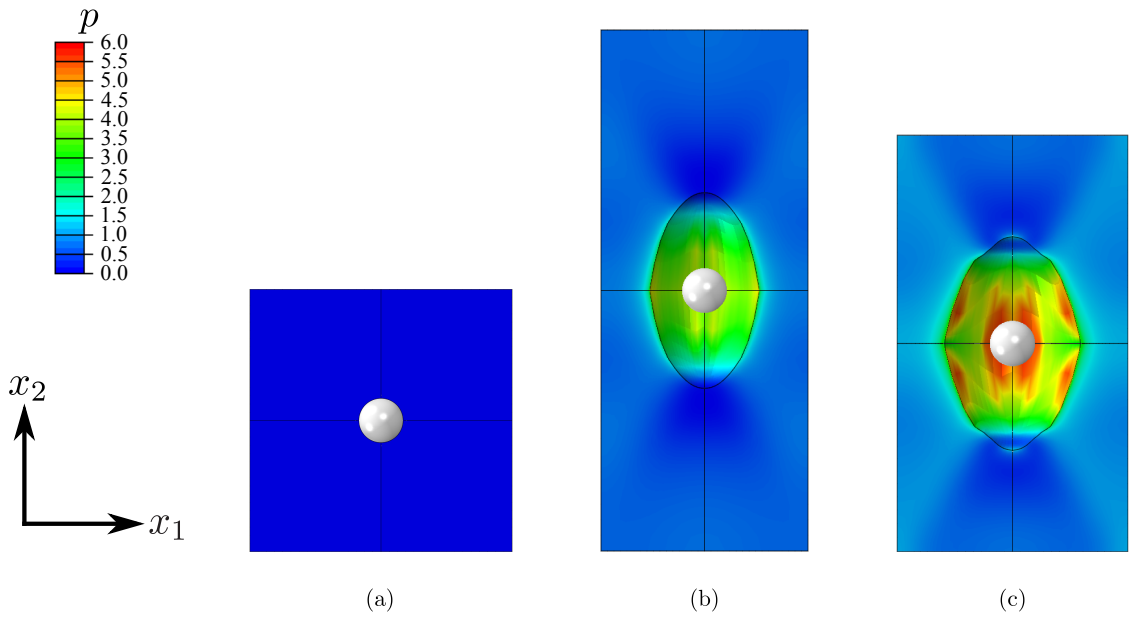

Figure 17: Initial and deformed configuration plots of the unit cell model with fringes of matrix accumulated plastic strain for the AA6082.25 alloy in temper O, depicted in the $x_1 - x_2$ (ED-TD) plane. (a) Initial configuration, (b) deformed configuration at onset of void coalescence after monotonic tension and (c) deformed configuration at the onset of void coalescence after 40% pre-compression. In the centre a (white) particle is shown.

Figure 18 depicts the void growth in terms of the normalised void volume fraction versus the accumulated von Mises strain for the unit cell model, where the current void volume fraction is defined as

$$f = \frac{V_{uc} - V_m}{V_{uc}} \tag{43}$$

Here, V_{uc} is the current volume of the unit cell and V_m is the current volume of the matrix material, i.e., the sum of all integration point volumes. The void growth is distinct and evolves differently after pre-compression for the different materials. After pre-compression the growth rate tends to be higher than for monotonic tension. This is the case for all the materials except the AA6082.25 alloy in T6 temper, where the void growth rate appears to decrease with increasing pre-compression after load reversal. For the AA6060 alloy in temper T7 and T6, the initial growth rate after load reversal is lower for the unit cell subjected to 40% pre-compression than monotonic tension, but after some straining the growth rate increases beyond that observed for monotonic tension. The critical void volume fraction, i.e., the void volume fraction at coalescence, is seen to increase with increasing pre-compression for all the materials. The point corresponding to coalescence is indicated with a cross in the figures.

The evolution of the void and particularly the void aspect ratios R_1/R_2 and R_3/R_2 can be seen in Figure 19. The void is prolate/oblate in the x_1-x_2 plane if the ratio R_1/R_2 is less/greater than unity. Similarly, a value of R_3/R_2 less/greater than unity implies a prolate/oblate void in the x_2-x_3 plane. The void aspect ratios have initial values equal to unity, i.e., a spherical void in the unit cell. The shape of the void for the unit cell subjected to monotonic tension evolves in the beginning of the deformation into a

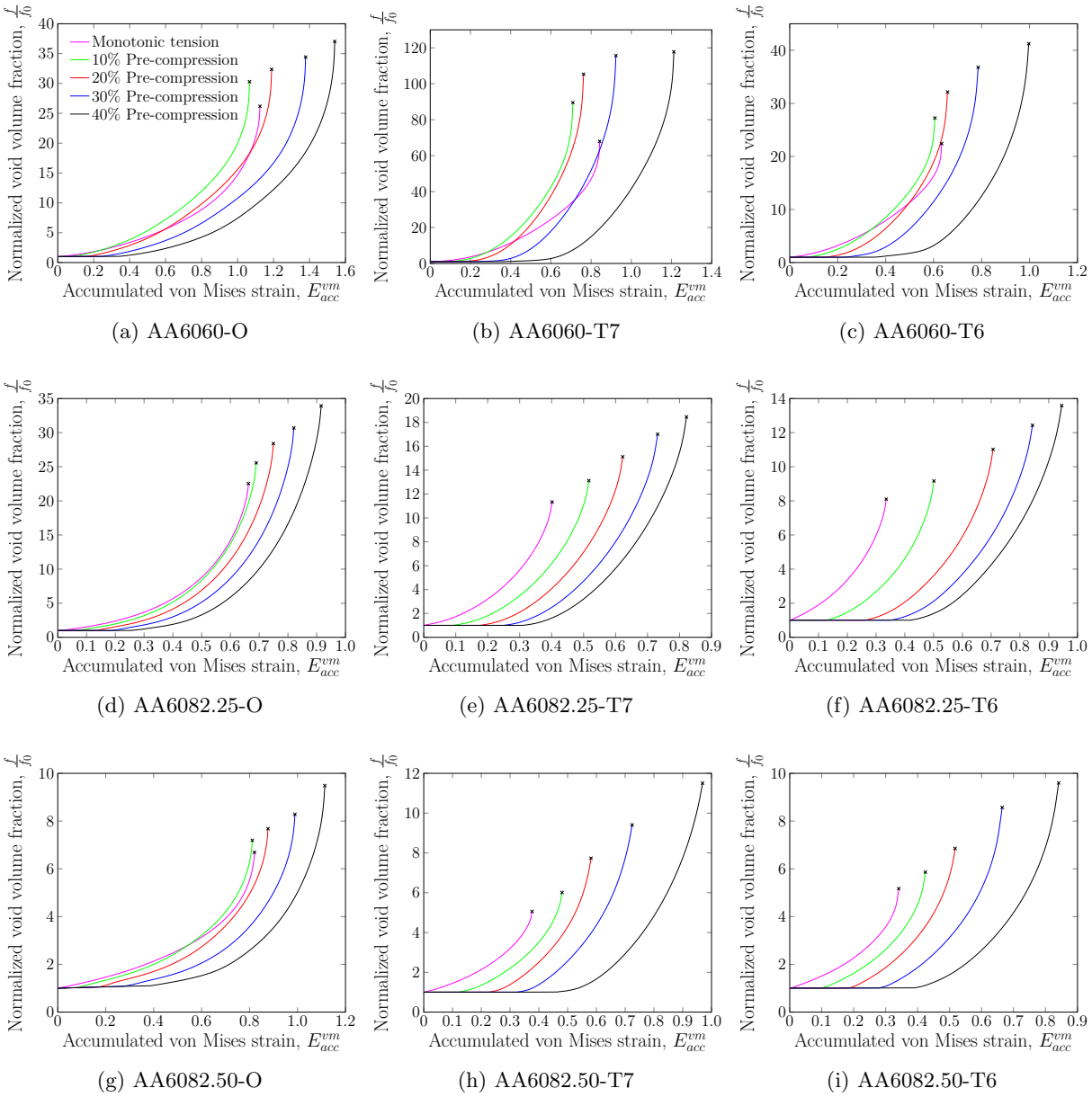

(a) AA6060-O (b) AA6060-T7 (c) AA6060-T6

(d) AA6082.25-O (e) AA6082.25-T7 (f) AA6082.25-T6

(g) AA6082.50-O (h) AA6082.50-T7 (i) AA6082.50-T6

Figure 18: Normalized void volume fraction versus the accumulated von Mises strain for the unit cell model. The point corresponding to coalescence is indicated with a cross.

prolate spheroid for all the materials. As deformation continues and close to coalescence, the void becomes prolate along one of the material directions and oblate in the other for some of the materials. This is typical for the AA6060 and AA6082.50 alloys in T7 and T6 temper, while the other materials preserve the prolate void shape until coalescence.

During compression the void is seen to separate from the particle for some of the materials in one of the directions normal to the compression axis (TD). This is observed for nearly all the materials except the AA6082.25 alloy in T7 and T6 temper. The amount of separation and when separation occurs are dependent upon the material. In particular, the AA6060 and AA6082.50 alloys in O temper are seen to exhibit separation from the beginning of the compression phase, as the void aspect ratio is greater than unity.

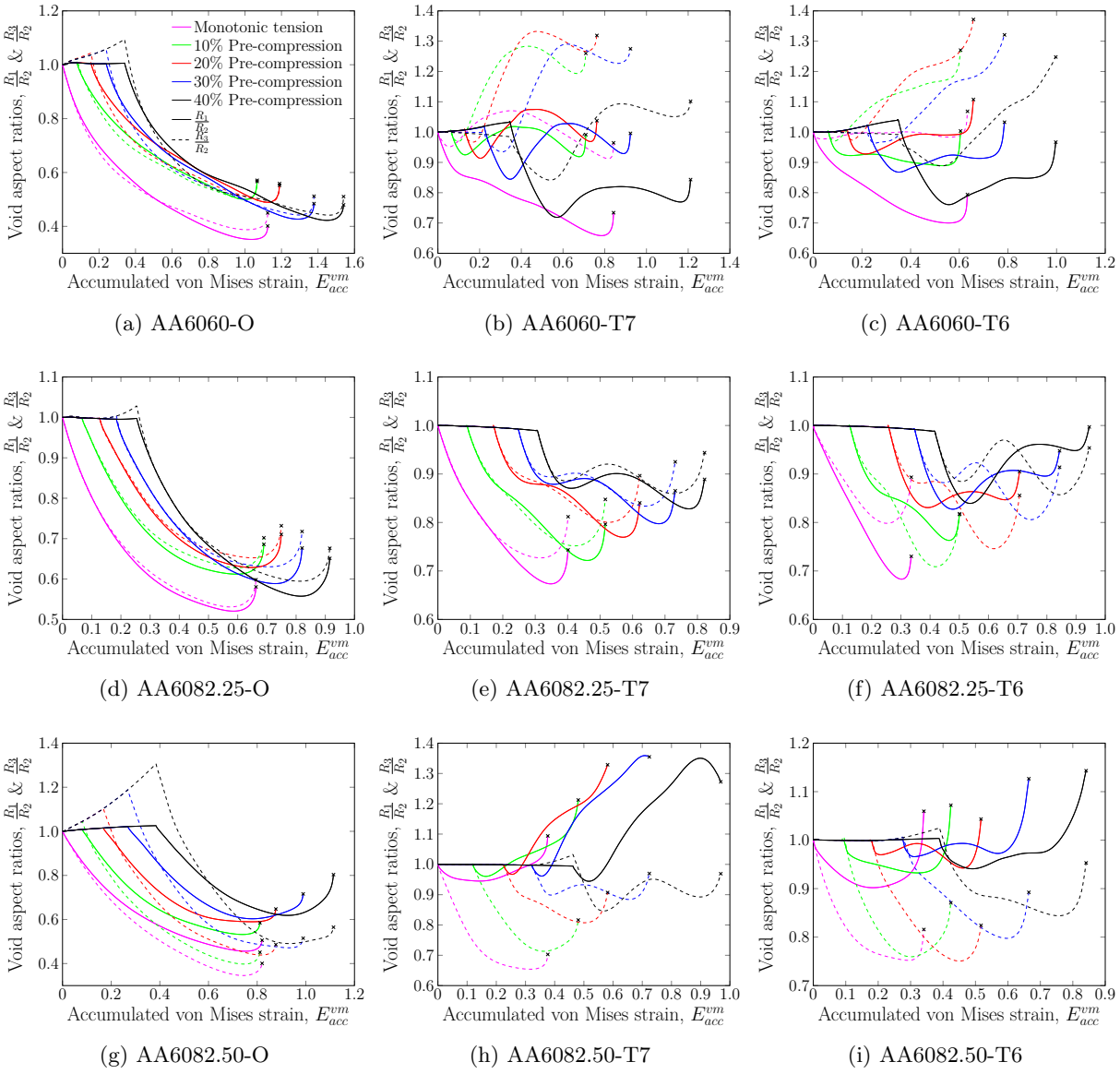

(a) AA6060-O (b) AA6060-T7 (c) AA6060-T6

(d) AA6082.25-O (e) AA6082.25-T7 (f) AA6082.25-T6

(g) AA6082.50-O (h) AA6082.50-T7 (i) AA6082.50-T6

Figure 19: Void aspect ratios versus the accumulated von Mises strain for the unit cell model. The point corresponding to coalescence is indicated with a cross.

In contrast, the AA6082.50 alloy in T7 and T6 temper only shows sign of separation after approximately 30% compression. After load reversal, the response is also different between alloys and from the response in monotonic tension. The materials exhibiting a prolate void shape along one material axis and an oblate void shape along the other axis for monotonic tension also exhibit this response after load reversal. This transition from a purely prolate shape to a combination of a prolate and oblate shape appears to occur after less deformation in tension after load reversal than for monotonic tension. The AA6060 and AA6082.50 alloys in temper T7 and T6 display a similar evolution of the void aspect ratio. The largest difference being that the oblate shape evolves along the x_3 axis (ND) for the AA6060 alloy, while it evolves along the x_1 axis (ED) for the AA6082.50 alloy. This is related to the anisotropy of these alloys, as the texture components of the Goss and the rotated cube texture for the AA6060 and AA6082.50 alloy, respectively, are related by a 90° rotation about the x_2 axis (TD).

We can now relate the accumulated von Mises strain at coalescence in the unit cell to that of the critical element of the diabolo-shaped specimen. Thus, we can find the logarithmic strain at coalescence, as calculated from the cross-section area of the specimen. Fracture initiation in the specimen predicted by the unit cell can then be compared to the experimental results. Figure 20 shows the failure strain and the relative failure strain versus pre-compression level for the experiments and the finite element analyses based on the unit cell simulations.

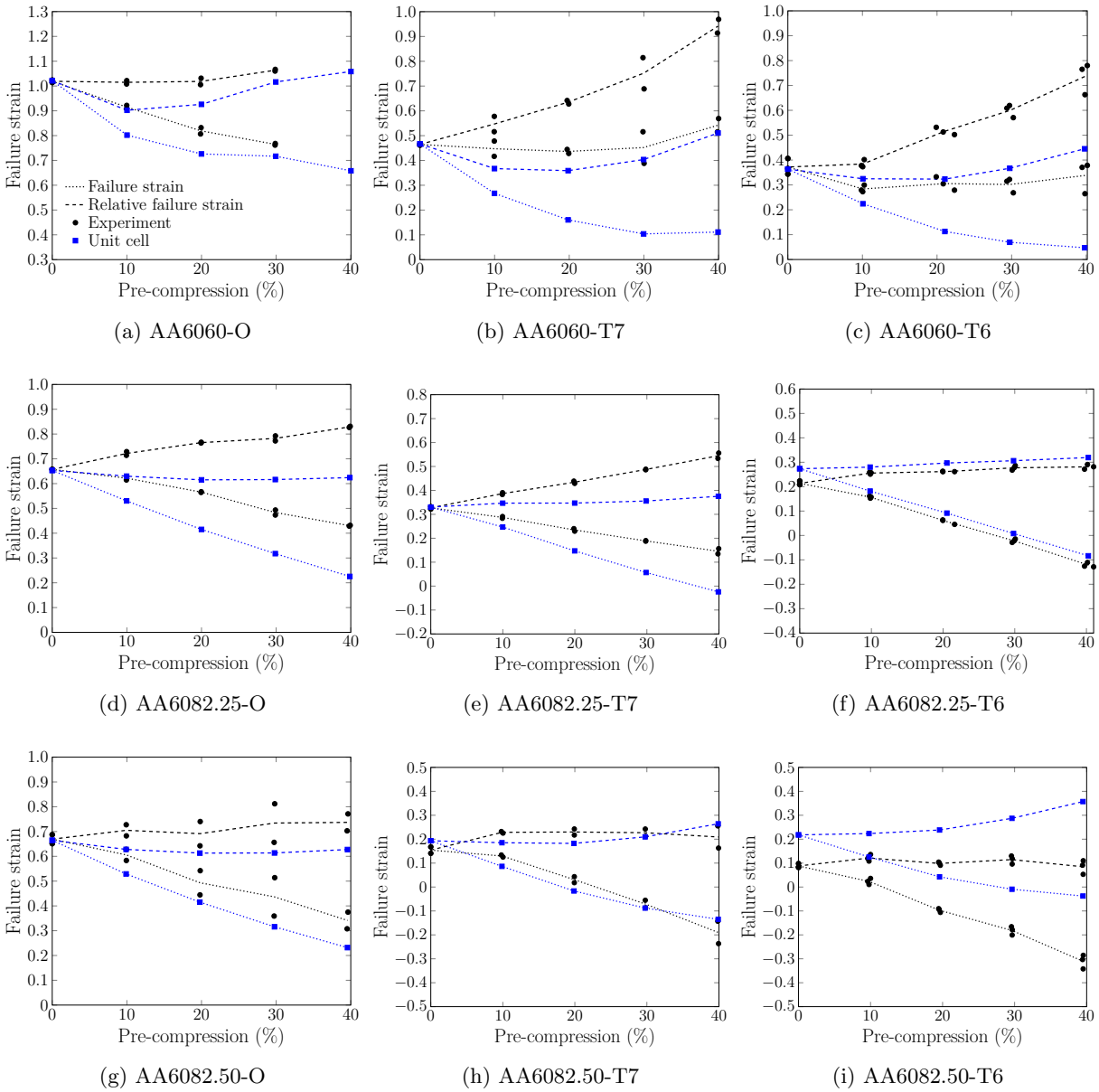

(a) AA6060-O (b) AA6060-T7 (c) AA6060-T6

(d) AA6082.25-O (e) AA6082.25-T7 (f) AA6082.25-T6

(g) AA6082.50-O (h) AA6082.50-T7 (i) AA6082.50-T6

Figure 20: Failure strain, ε_f, and relative failure strain, ε_r, versus pre-compression level from experiments and finite element analyses of unit cells. The relative failure strain is the strain to failure measured with respect to the compressed configuration.

Studying the results for the AA6060 alloy in Figure 20, it is observed that the predicted relative failure strain decreases from 0 to 10% pre-compression for all the tempers, unlike in the experiments. Then, the predicted relative failure strain increases for further pre-compression for the AA6060 alloy in temper O, whereas it decreases until 20% pre-compression before it increases again for the AA6060 alloy in temper

T7 and T6. It is clear that the applied unit cell model is incapable of predicting the large increase in the relative failure strain with increasing pre-compression as observed in the experiments. For the AA6060 alloy in temper O, the predictions are closer to the experimental results. This indicates that there are also other mechanisms involved in the fracture process than those included in the unit cell model that are particularly important for the T7 and T6 tempers of this alloy, see Section 6. Considering the results for the AA6082.25 alloy in Figure 20, it is seen that the simulations predict an almost constant or a small increase in the relative failure strain with increasing pre-compression for all the tempers. A small increase is observed for the AA6082.25 alloy in temper T7 and T6, and the evolution predicted for the T6 temper is approximately equal to that observed in the experiments. The failure strain is higher in monotonic tension in the simulations than in the experiments for this material. This is because the initial void/particle fraction of the unit cell was restricted by the measured particle fraction for the AA6082.25 alloy in T6 temper and the AA6082.50 alloy in T7 and T6 tempers. Again this indicates that there are also other mechanisms involved in the fracture process, as will be discussed in Section 6. For the AA6082.50 alloy in Figure 20, it is observed that the predicted relative failure strain is approximately constant for all the tempers with increasing pre-compression. This is in agreement with the experiments.

6. Discussion

From the experimental results presented in Figure 2, significant differences are observed in the tensile ductility between the alloys and between the tempers within the same alloy. While the grain structure and anisotropy differ between the alloys, they are similar for the different tempers of the same alloy. In contrast, the strength and work-hardening behaviour depends markedly on the tempering and it transpires that these characteristics are important for the tensile ductility of an alloy. Figure 3 clearly suggests that the ductility of the materials in monotonic tension depends upon their yield strength. Previous studies indicate that the failure strain decreases linearly with increasing yield strength for aluminium alloys with similar microstructures (Lloyd, 2003; Westermann et al., 2014; Pedersen et al., 2015; Hannard et al., 2016). In Figure 2, pre-compression is found to either increase the tensile ductility compared to monotonic tension or to leave it approximately constant. In contrast, Bao and Treitler (2004) observed a decrease in the tensile ductility for an AA2024-T351 aluminium alloy with increasing pre-compression, and attributed the reduction in tensile ductility to particle fracture and an increased dislocation density after pre-compression. For an X65 steel, a decrease in tensile ductility has been observed after pre-compression as the failure mechanism may change from ductile to brittle (Kristoffersen et al., 2013).

For the AA6060 alloy in T7 and T6 temper, areas of intercrystalline fracture were observed on the fracture surface (Frodal et al., 2017). After pre-compression, the amount of intercrystalline fracture was found to decrease with increasing pre-compression, leading to an increase in the tensile ductility for these materials. On the other hand, intercrystalline fracture was not observed for the AA6060 alloy in temper O, and the amount of intercrystalline fracture for the AA6082.25 alloy was not seen to change after pre-compression. The precipitation free zones (PFZs) located adjacent to the grain boundaries are assumed to be the cause of intercrystalline fracture in these alloys (Lohne and Naess, 1979). In these weaker zones, the plastic deformation can localise, and crack initiation and growth may occur more easily (Dowling and Martin, 1976; Morgeneyer et al., 2008; Khadyko et al., 2016b). A possible reason for the reduced amount of intercrystalline fracture in the AA6060 alloy in temper T7 and T6 after pre-compression is strengthening of the PFZs during compression (Christiansen et al., 2018).

When using polycrystal plasticity calculations to predict the yield surface of a material, the crystal plasticity model and the calibrated yield surface are in most cases not capable of precisely capturing all experimental observations, although good agreement has been obtained when more refined representations of the polycrystal aggregate are used (Zhang et al., 2015; Zhang et al., 2016). In the present study, the yield surfaces calibrated from crystal plasticity finite element simulations are deemed sufficiently accurate. The plastic anisotropy is generally overestimated for the AA6060 and AA6082.50 alloys, while the response of the AA6082.25 alloy is captured accurately, as seen by comparing Table 3 and Table 11. However, this comparison gives only an indication on the performance of the calibrated yield surfaces, as more experimental tests are needed for a complete assessment. Although the main source of anisotropy is the crystallographic

texture of a material (Engler and Randle, 2009), the grain morphology may have a noticeable effect (Delannay et al., 2009). The AA6060 alloy investigated here has a recrystallised, equi-axed grain structure and the RVE used in the crystal plasticity finite element simulations represents this morphology with reasonable accuracy. In contrast, the RVE gives a less accurate description of the fibrous grain structure for the AA6082.25 alloy, while the calibrated yield surfaces for this alloy appear to be more accurate based on the limited experimental validation. Using a higher resolution mesh could have resolved the inter-grain gradients and given a more accurate description of the underlying microstructure, but at the cost of significantly increasing the computational time.

During plastic deformation the crystallographic texture in the deformed area of the specimens will evolve and affect the shape of the yield surface. Preliminary crystal plasticity finite element calculations of the materials suggest that during compression the cube texture component of the AA6060 and AA6082.25 alloys weakens. In contrast, the rotated cube texture of the AA6082.50 alloy strengthens during compression. In the subsequent tension stage, the trends are reversed and the texture of the AA6060 and AA6082.25 strengthens, whereas it weakens for the AA6082.50 alloy. Thus, when the strain is back to zero, the texture is similar to the initial texture of the alloy.

The strain path change model proposed by Mánik et al. (2015) captures the main effects of the strain reversal with reasonable accuracy, cf. Figure 11. However, the model is incapable of describing the evolution of the work-hardening stagnation with increasing pre-compression observed for the alloys in temper O. It is seen in Figure 12 that accurate modelling of the strain reversal effects is particularly important for the stress level after load-reversal and close to failure, which would otherwise be highly overestimated. An accurate description of the loading history and the void growth rate depends critically on the hardening behaviour (Lecarme et al., 2011).

In Figure 13 and Figure 14, differences in the loading histories are observed between the alloys and between the different tempers of the same alloy. This is clearly observed for the AA6060 alloy, as the stress triaxiality is significantly lower in magnitude for the O temper than for the two other tempers. The triaxiality level is also lower for the other alloys in temper O, where the work hardening of the materials is the largest. Thus, the high work hardening of the O tempers reduces the triaxiality level and leads to an increased failure strain in monotonic tension. After pre-compression, the work-hardening stagnation observed for the alloys in temper O leads to plastic localisation and increased triaxiality. In addition, the compression of the specimen leads to a lower curvature of the neck, thus reducing the triaxiality after re-yielding in tension. It is reasonable to expect that the work-hardening stagnation reduces the failure strain, while the lower curvature of the neck after pre-compression has the opposite effect.

The loading history is also affected by the plastic anisotropy. For the stress triaxiality ratio, the effect of anisotropy seems to be as large as the effect of strength and work hardening. In contrast, the effect of anisotropy on the deviatoric angle appears to be even larger than that of the strength and work hardening. Thus, the anisotropy affects the location of yielding in stress space, as observed in the deviatoric plane. The anisotropy also affects the void aspect ratio, see Figure 19, and for the materials with the highest strength and lowest work hardening the influence is seen to be the largest.

From the results of the unit cell simulations, see Figure 20, it is found that the unit cell model predicts an almost constant tensile ductility after pre-compression. Albeit the strength, work hardening and anisotropy vary between the different materials, the failure mechanism described by the unit cell model is the same, namely growth and coalescence of a uniform distribution of pre-nucleated voids with equally sized particles inside. The prediction of an almost constant tensile ductility matches the experimental observations for some of the materials. In addition, other physical mechanisms will play an important role in the ductile failure process. The large grains observed for the AA6082.50 alloy will have an effect on the strain to failure and are critical in the ductile failure process, as the large grains increase the likelihood of intercrystalline fracture and reduce the ductility of the alloy (Frodal et al., 2017).

The unit cell adopted in the present study represents materials consisting of a matrix and pre-nucleated voids with particles inside. In the actual materials, a combination of initial voids, with and without particles inside, and differently shaped particles, with and without cohesion to the matrix material, is observed (Frodal et al., 2017). During the extrusion process, primary particles have been observed to crack and debond from the matrix, leading to a diversity of pre-nucleated voids in the vicinity of particles. When the material is

deformed in compression, voids without particles inside, voids in the vicinity of smaller particles and voids between cracked particles may shrink and close any gaps between the matrix and particle and between cracked particles. This delays the void growth in the subsequent tension stage and leads to increased tensile ductility.

Another effect not accounted for in the unit cell model is the influence of nucleation and debonding of the particle from the matrix material. During compression, the cohesion between the particle and matrix may increase or decrease depending on the underlying physical mechanisms present at the interface. The void growth rate in the unit cell model after load reversal was observed to be initially lower than that for monotonic tension for the AA6060 alloy in temper T7 and T6, see Figure 18. If nucleation was accounted for, e.g., by including a cohesive zone between the matrix and particle, this would possibly reduce the nucleation rate after pre-compression and lead to an increase in the tensile ductility. In contrast, particles can crack during the compression phase and create new free surfaces where voids may grow during the tension stage (Bao and Treitler, 2004). This mechanism is more probable for the alloys with the highest strength, and the result is lower tensile ductility. A combination of all the above-mentioned mechanisms is probably in operation during the ductile failure process, and the importance of a certain mechanism will be different depending on the alloy and temper combination.

7. Concluding remarks

The influence of reversed loading on ductile failure for three aluminium alloys heat-treated to three different tempers was studied by conducting reversed loading experiments and finite element unit cell simulations. Diabolo-shaped specimens machined from extruded profiles were subjected to five different pre-compression levels and pulled to fracture in tension. The three aluminium alloys used herein, i.e., AA6060, AA6082.25 and AA6082.50, had different grain structure, grain size and crystallographic texture, and the strength and work hardening varied between the alloys and with the heat treatment. The strain to failure in monotonic tension was seen to decrease with increasing initial yield strength. After pre-compression, the tensile ductility is largely constant or exhibits a small increase for the majority of the materials, but for some materials a larger increase is observed with increasing pre-compression level. Here, tensile ductility is defined as the deformation capacity of a material after the pre-deformation.

The yield surfaces determined by crystal plasticity finite element simulations give a fair representation of the plastic anisotropy. For some of the materials the anisotropy is overestimated, but the adopted hierarchical modelling framework is nonetheless promising. The importance of a plasticity model accounting for transient and permanent effects after a strain reversal is demonstrated, as isotropic hardening or combined isotropic and kinematic hardening is not sufficient to describe the stress-strain curves observed experimentally after the strain reversal.

In general, the unit cell simulations predict a largely constant tensile ductility with pre-compression, and the strength, work hardening and anisotropy of the materials are found to have only a minor influence on the effect of pre-compression, i.e., only a minor effect is observed on the evolution of the relative failure strain with pre-compression. In contrast, the strength, work hardening and anisotropy have a larger influence on the deformation of the unit cell, and on the ductility in monotonic tension. Depending on the alloy and temper, other physical mechanisms that are not accounted for in the unit cell model can have a significant influence on the ductile failure process, e.g., inter-crystalline fracture induced by precipitate free zones along the grain boundaries. Inter-crystalline fracture is difficult to account for in the current unit cell framework and a localisation approach using imperfection analyses could be more appropriate to study this failure mechanism. Thus, further work will focus on simulations of the reversed loading experiments by imperfection analysis.

Acknowledgements

The financial support of this work from the Centre for Advanced Structural Analysis (CASA), Project No. 237885, Centre for Research-based Innovation (CRI) at the Norwegian University of Science and Technology (NTNU), is gratefully acknowledged.

References

Abaqus, 2014. Version 6.14. Dassault Systemès Simulia Corporation. Providence, Rhode Island, USA.

An, Y., Vegter, H., Carless, L., Lambriks, M., 2011. A novel yield locus description by combining the taylor and the relaxed taylor theory for sheet steels. International Journal of Plasticity 27, 1758 – 1780.

Aretz, H., 2008. A simple isotropic-distortional hardening model and its application in elastic–plastic analysis of localized necking in orthotropic sheet metals. International Journal of Plasticity 24, 1457 – 1480.

Aretz, H., Aegerter, J., Engler, O., 2010. Analysis of earing in deep drawn cups. AIP Conference Proceedings 1252, 417–424.

Aretz, H., Barlat, F., 2013. New convex yield functions for orthotropic metal plasticity. International Journal of Non-Linear Mechanics 51, 97 – 111.

Armstrong, P.J., Frederick, C.O., 1966. A mathematical representation of the multiaxial Bauschinger effect. Technical Report. RD/B/N731, CEGB, Central Electricity Generating Board, Berkeley, UK.

Bai, Y., Wierzbicki, T., 2008. A new model of metal plasticity and fracture with pressure and lode dependence. International Journal of Plasticity 24, 1071 – 1096.

Bao, Y., Treitler, R., 2004. Ductile crack formation on notched Al2024-T351 bars under compression–tension loading . Materials Science and Engineering: A 384, 385 – 394.

Barlat, F., Aretz, H., Yoon, J.W., Karabin, M.E., Brem, J.C., Dick, R.E., 2005. Linear transfomation-based anisotropic yield functions. International Journal of Plasticity 21, 1009 – 1039.

Barlat, F., Grácio, J.J., Lee, M.G., Rauch, E.F., Vincze, G., 2011. An alternative to kinematic hardening in classical plasticity. International Journal of Plasticity 27, 1309 – 1327.

Barlat, F., Ha, J., Grácio, J.J., Lee, M.G., Rauch, E.F., Vincze, G., 2013. Extension of homogeneous anisotropic hardening model to cross-loading with latent effects. International Journal of Plasticity 46, 130 – 142.

Barlat, F., Lege, D.J., Brem, J.C., 1991. A six-component yield function for anisotropic materials. International Journal of Plasticity 7, 693 – 712.

Barlat, F., Vincze, G., Grácio, J.J., Lee, M.G., Rauch, E.F., Tomé, C.N., 2014. Enhancements of homogenous anisotropic hardening model and application to mild and dual-phase steels. International Journal of Plasticity 58, 201 – 218.

Barsoum, I., Faleskog, J., 2007. Rupture mechanisms in combined tension and shear—micromechanics. International Journal of Solids and Structures 44, 5481 – 5498.

Basu, S., Benzerga, A.A., 2015. On the path-dependence of the fracture locus in ductile materials: Experiments. International Journal of Solids and Structures 71, 79 – 90.

Bauschinger, J., 1881. Changes of the elastic limit and the modulus of elasticity on various metals. Zivilingenieur 27, 289–348.

Benzerga, A.A., Besson, J., 2001. Plastic potentials for anisotropic porous solids. European Journal of Mechanics - A/Solids 20, 397 – 434.

Benzerga, A.A., Surovik, D., Keralavarma, S.M., 2012. On the path-dependence of the fracture locus in ductile materials – analysis. International Journal of Plasticity 37, 157 – 170.

Bishop, J.F.W., Hill, R., 1951a. A theory of the plastic distortion of a polycrystalline aggregate under combined stresses. Philosophical Magazine 42, 414–427.

Bishop, J.F.W., Hill, R., 1951b. A theoretical derivation of the plastic properties of a polycrystalline face-centred metal. Philosophical Magazine 42, 1298–1307.

Bron, F., Besson, J., 2004. A yield function for anisotropic materials application to aluminum alloys. International Journal of Plasticity 20, 937 – 963.

Bulatov, V.V., Richmond, O., Glazov, M.V., 1999. An atomistic dislocation mechanism of pressure-dependent plastic flow in aluminum. Acta Materialia 47, 3507 – 3514.

Cazacu, O., Barlat, F., 2001. Generalization of Drucker's Yield Criterion to Orthotropy. Mathematics and Mechanics of Solids 6, 613–630.

Cheng, L., Guo, T.F., 2007. Void interaction and coalescence in polymeric materials. International Journal of Solids and Structures 44, 1787 – 1808.

Chien, W.Y., Pan, J., Tang, S.C., 2001. Modified anisotropic gurson yield criterion for porous ductile sheet metals. Journal of engineering materials and technology 123, 409–416.

Christiansen, E., Marioara, C.D., Marthinsen, K., Hopperstad, O.S., Holmestad, R., 2018. Lattice rotations in precipitate free zones in an Al-Mg-Si alloy. Materials Characterization 144, 522 – 531.

Delannay, L., Melchior, M.A., Signorelli, J.W., Remacle, J.F., Kuwabara, T., 2009. Influence of grain shape on the planar anisotropy of rolled steel sheets – evaluation of three models. Computational Materials Science 45, 739 – 743.

Dæhli, L.E.B., Børvik, T., Hopperstad, O.S., 2016a. Influence of loading path on ductile fracture of tensile specimens made from aluminium alloys. International Journal of Solids and Structures 88, 17 – 34.

Dæhli, L.E.B., Faleskog, J., Børvik, T., Hopperstad, O.S., 2016b. Unit cell simulations and porous plasticity modelling for recrystallization textures in aluminium alloys. Procedia Structural Integrity 2, 2535 – 2542. 21st European Conference on Fracture, ECF21, 20-24 June 2016, Catania, Italy.

Dæhli, L.E.B., Faleskog, J., Børvik, T., Hopperstad, O.S., 2017. Unit cell simulations and porous plasticity modelling for strongly anisotropic fcc metals. European Journal of Mechanics - A/Solids 65, 360 – 383.

Dowling, J.M., Martin, J.W., 1976. The influence of MN additions on the deformation behaviour of an Al-Mg-Si alloy. Acta Metallurgica 24, 1147 – 1153.

Drucker, D.C., Prager, W., 1952. Soil mechanics and plastic analysis or limit design. Quarterly of applied mathematics 10, 157–165.

Eisenlohr, P., Diehl, M., Lebensohn, R.A., Roters, F., 2013. A spectral method solution to crystal elasto-viscoplasticity at finite strains. International Journal of Plasticity 46, 37 – 53.

Engler, O., Randle, V., 2009. Introduction to texture analysis: macrotexture, microtexture, and orientation mapping. Second ed., CRC press, Taylor & Francis Group.

Faleskog, J., Gao, X., Shih, C.F., 1998. Cell model for nonlinear fracture analysis – I. Micromechanics calibration. International Journal of Fracture 89, 355–373.

Fourmeau, M., Børvik, T., Benallal, A., Lademo, O.G., Hopperstad, O.S., 2011. On the plastic anisotropy of an aluminium alloy and its influence on constrained multiaxial flow. International Journal of Plasticity 27, 2005 – 2025.

François, M., 2001. A plasticity model with yield surface distortion for non proportional loading. International Journal of Plasticity 17, 703 – 717.

Frederick, C.O., Armstrong, P.J., 2007. A mathematical representation of the multiaxial bauschinger effect. Materials at High Temperatures 24, 1–26.

Freund, M., Shutov, A.V., Ihlemann, J., 2012. Simulation of distortional hardening by generalizing a uniaxial model of finite strain viscoplasticity. International Journal of Plasticity 36, 113 – 129.

Frodal, B.H., Pedersen, K.O., Børvik, T., Hopperstad, O.S., 2017. Influence of pre-compression on the ductility of AA6xxx aluminium alloys. International Journal of Fracture 206, 131–149.

Gawad, J., Banabic, D., Bael, A.V., Comsa, D.S., Gologanu, M., Eyckens, P., Houtte, P.V., Roose, D., 2015. An evolving plane stress yield criterion based on crystal plasticity virtual experiments. International Journal of Plasticity 75, 141 – 169.

Groeber, M.A., Jackson, M.A., 2014. DREAM.3D: A Digital Representation Environment for the Analysis of Microstructure in 3D. Integrating Materials and Manufacturing Innovation 3, 5.

Grytten, F., Holmedal, B., Hopperstad, O.S., Børvik, T., 2008. Evaluation of identification methods for Yld2004-18p. International Journal of Plasticity 24, 2248 – 2277.

Ha, J., Lee, M.G., Barlat, F., 2013. Strain hardening response and modeling of EDDQ and DP780 steel sheet under non-linear strain path. Mechanics of Materials 64, 11 – 26.

Hannard, F., Pardoen, T., Maire, E., Bourlot, C.L., Mokso, R., Simar, A., 2016. Characterization and micromechanical modelling of microstructural heterogeneity effects on ductile fracture of 6xxx aluminium alloys. Acta Materialia 103, 558 – 572.

Hasegawa, T., Yakou, T., Kocks, U.F., 1986. Forward and reverse rearrangements of dislocations in tangled walls. Materials Science and Engineering 81, 189 – 199.

Hershey, A.V., 1954. The plasticity of an isotropic aggregate of anisotropic face-centered cubic crystals. Journal of Applied Mechanics 21, 241–249.

Hill, R., 1948. A theory of the yielding and plastic flow of anisotropic metals. Proceedings of the Royal Society of London A: Mathematical, Physical and Engineering Sciences 193, 281–297.

Holmedal, B., Houtte, P.V., An, Y., 2008. A crystal plasticity model for strain-path changes in metals. International Journal of Plasticity 24, 1360 – 1379.

Holmen, J.K., Frodal, B.H., Hopperstad, O.S., Børvik, T., 2017. Strength differential effect in age hardened aluminum alloys. International Journal of Plasticity 99, 144 – 161.

Hosford, W.F., 1972. A generalized isotropic yield criterion. Journal of Applied Mechanics 39, 607–609.

Hutchinson, J.W., 1976. Bounds and self-consistent estimates for creep of polycrystalline materials. Proceedings of the Royal Society of London A: Mathematical, Physical and Engineering Sciences 348, 101–127.

Iadicola, M.A., Foecke, T., Banovic, S.W., 2008. Experimental observations of evolving yield loci in biaxially strained AA5754-O. International Journal of Plasticity 24, 2084 – 2101.

Inal, K., Mishra, R.K., Cazacu, O., 2010. Forming simulation of aluminum sheets using an anisotropic yield function coupled with crystal plasticity theory. International Journal of Solids and Structures 47, 2223 – 2233.

Kanjarla, A.K., Van Houtte, P., Delannay, L., 2010. Assessment of plastic heterogeneity in grain interaction models using crystal plasticity finite element method. International Journal of Plasticity 26, 1220 – 1233.

Karafillis, A.P., Boyce, M.C., 1993. A general anisotropic yield criterion using bounds and a transformation weighting tensor. Journal of the Mechanics and Physics of Solids 41, 1859 – 1886.

Keralavarma, S.M., Benzerga, A.A., 2010. A constitutive model for plastically anisotropic solids with non-spherical voids. Journal of the Mechanics and Physics of Solids 58, 874 – 901.

Keralavarma, S.M., Hoelscher, S., Benzerga, A.A., 2011. Void growth and coalescence in anisotropic plastic solids. International Journal of Solids and Structures 48, 1696 – 1710.

Khadyko, M., 2018. Personal communication. Structural Impact Laboratory (SIMLab), Norwegian University of Science and Technology (NTNU).

Khadyko, M., Dumoulin, S., Børvik, T., Hopperstad, O.S., 2014. An experimental–numerical method to determine the work-hardening of anisotropic ductile materials at large strains. International Journal of Mechanical Sciences 88, 25 – 36.

Khadyko, M., Dumoulin, S., Børvik, T., Hopperstad, O.S., 2015. Simulation of large-strain behaviour of aluminium alloy under tensile loading using anisotropic plasticity models. Computers & Structures 157, 60 – 75.

Khadyko, M., Dumoulin, S., Cailletaud, G., Hopperstad, O.S., 2016a. Latent hardening and plastic anisotropy evolution in AA6060 aluminium alloy. International Journal of Plasticity 76, 51 – 74.

Khadyko, M., Marioara, C.D., Ringdalen, I.G., Dumoulin, S., Hopperstad, O.S., 2016b. Deformation and strain localization in polycrystals with plastically heterogeneous grains. International Journal of Plasticity 86, 128 – 150.

Khan, A.S., Huang, S., 1995. Continuum theory of plasticity. John Wiley & Sons.

Khan, A.S., Kazmi, R., Pandey, A., Stoughton, T., 2009. Evolution of subsequent yield surfaces and elastic constants with finite plastic deformation. Part-I: A very low work hardening aluminum alloy (Al6061-T6511). International Journal of Plasticity

25, 1611 – 1625.
Khan, A.S., Pandey, A., Stoughton, T., 2010a. Evolution of subsequent yield surfaces and elastic constants with finite plastic deformation. Part II: A very high work hardening aluminum alloy (annealed 1100 Al). International Journal of Plasticity 26, 1421 – 1431.
Khan, A.S., Pandey, A., Stoughton, T., 2010b. Evolution of subsequent yield surfaces and elastic constants with finite plastic deformation. Part III: Yield surface in tension–tension stress space (Al 6061–T 6511 and annealed 1100 Al). International Journal of Plasticity 26, 1432 – 1441.
Kim, J., Gao, X., Srivatsan, T.S., 2004. Modeling of void growth in ductile solids: effects of stress triaxiality and initial porosity. Engineering Fracture Mechanics 71, 379 – 400.
Kitayama, K., Tomé, C.N., Rauch, E.F., Grácio, J.J., Barlat, F., 2013. A crystallographic dislocation model for describing hardening of polycrystals during strain path changes. application to low carbon steels. International Journal of Plasticity 46, 54 – 69.
Kocks, U.F., Chandra, H., 1982. Slip geometry in partially constrained deformation. Acta Metallurgica 30, 695 – 709.
Kohar, C.P., Bassani, J.L., Brahme, A., Muhammad, W., Mishra, R.K., Inal, K., 2017. A new multi-scale framework to incorporate microstructure evolution in phenomenological plasticity: Theory, explicit finite element formulation, implementation and validation. International Journal of Plasticity doi:https://doi.org/10.1016/j.ijplas.2017.08.006.
Koplik, J., Needleman, A., 1988. Void growth and coalescence in porous plastic solids. International Journal of Solids and Structures 24, 835–853.
Kristoffersen, M., Børvik, T., Hopperstad, O.S., 2016. Using unit cell simulations to investigate fracture due to compression–tension loading. Engineering Fracture Mechanics 162, 269 – 289.
Kristoffersen, M., Børvik, T., Westermann, I., Langseth, M., Hopperstad, O.S., 2013. Impact against X65 steel pipes – An experimental investigation. International Journal of Solids and Structures 50, 3430 – 3445.
Lebensohn, R.A., Kanjarla, A.K., Eisenlohr, P., 2012. An elasto-viscoplastic formulation based on fast fourier transforms for the prediction of micromechanical fields in polycrystalline materials. International Journal of Plasticity 32-33, 59 – 69.
Lebensohn, R.A., Tomé, C.N., 1993. A self-consistent anisotropic approach for the simulation of plastic deformation and texture development of polycrystals: Application to zirconium alloys. Acta Metallurgica et Materialia 41, 2611 – 2624.
Lebensohn, R.A., Tomé, C.N., 1994. A self-consistent viscoplastic model: prediction of rolling textures of anisotropic polycrystals. Materials Science and Engineering: A 175, 71 – 82.
Lecarme, L., Tekoğlu, C., Pardoen, T., 2011. Void growth and coalescence in ductile solids with stage III and stage IV strain hardening. International Journal of Plasticity 27, 1203 – 1223.
Lee, E.H., Stoughton, T.B., Yoon, J.W., 2017. A yield criterion through coupling of quadratic and non-quadratic functions for anisotropic hardening with non-associated flow rule. International Journal of Plasticity 99, 120 – 143.
Lee, J., Kim, D., Lee, Y.S., Bong, H.J., Barlat, F., Lee, M.G., 2015. Stress update algorithm for enhanced homogeneous anisotropic hardening model. Computer Methods in Applied Mechanics and Engineering 286, 63 – 86.
Legarth, B.N., Tvergaard, V., 2018. Effects of plastic anisotropy and void shape on full three-dimensional void growth. Journal of Applied Mechanics 85, 051007.
Li, F., Bate, P.S., 1991. Strain path change effects in cube textured aluminium sheet. Acta Metallurgica et Materialia 39, 2639 – 2650.
Liu, Z.G., Wong, W.H., Guo, T.F., 2016. Void behaviors from low to high triaxialities: Transition from void collapse to void coalescence. International Journal of Plasticity 84, 183 – 202.
Lloyd, D.J., 2003. The scaling of the tensile ductile fracture strain with yield strength in Al alloys . Scripta Materialia 48, 341 – 344.
Lohne, O., Naess, O.J., 1979. The Effect of Dispersoids and Grain Size on Mechanical Properties of AlMgSi Alloys, in: Haasen, P., Gerold, V., Kostorz, G. (Eds.), Strength of Metals and Alloys. Pergamon, pp. 781 – 788.
Lou, Y., Yoon, J.W., 2018. Anisotropic yield function based on stress invariants for BCC and FCC metals and its extension to ductile fracture criterion. International Journal of Plasticity 101, 125 – 155.
Luo, M., Rousselier, G., 2014. Modeling of large strain multi-axial deformation of anisotropic metal sheets with strength-differential effect using a reduced texture methodology. International Journal of Plasticity 53, 66 – 89.
Mánik, T., Holmedal, B., Hopperstad, O.S., 2015. Strain-path change induced transients in flow stress, work hardening and r-values in aluminum. International Journal of Plasticity 69, 1 – 20.
Marcadet, S.J., Mohr, D., 2015. Effect of compression–tension loading reversal on the strain to fracture of dual phase steel sheets. International Journal of Plasticity 72, 21 – 43.
Molinari, A., Canova, G.R., Ahzi, S., 1987. A self consistent approach of the large deformation polycrystal viscoplasticity. Acta Metallurgica 35, 2983 – 2994.
Morgeneyer, T.F., Starink, M.J., Wang, S.C., Sinclair, I., 2008. Quench sensitivity of toughness in an Al alloy: Direct observation and analysis of failure initiation at the precipitate-free zone. Acta Materialia 56, 2872 – 2884.
Pandey, A., Khan, A.S., Kim, E.Y., Choi, S.H., Gnäupel-Herold, T., 2013. Experimental and numerical investigations of yield surface, texture, and deformation mechanisms in AA5754 over low to high temperatures and strain rates. International Journal of Plasticity 41, 165 – 188.
Papasidero, J., Doquet, V., Mohr, D., 2015. Ductile fracture of aluminum 2024-T351 under proportional and non-proportional multi-axial loading: Bao–Wierzbicki results revisited. International Journal of Solids and Structures 69, 459 – 474.
Pedersen, K.O., Westermann, I., Furu, T., Børvik, T., Hopperstad, O.S., 2015. Influence of microstructure on work-hardening and ductile fracture of aluminium alloys . Materials & Design 70, 31 – 44.
Plunkett, B., Cazacu, O., Lebensohn, R.A., Barlat, F., 2007. Elastic-viscoplastic anisotropic modeling of textured metals and validation using the taylor cylinder impact test. International Journal of Plasticity 23, 1001 – 1021.

Qin, J., Holmedal, B., Hopperstad, O.S., 2018. A combined isotropic, kinematic and distortional hardening model for aluminum and steels under complex strain-path changes. International Journal of Plasticity 101, 156 – 169.

Qin, J., Holmedal, B., Zhang, K., Hopperstad, O.S., 2017. Modeling strain-path changes in aluminum and steel. International Journal of Solids and Structures 117, 123 – 136.

Raabe, D., Roters, F., 2004. Using texture components in crystal plasticity finite element simulations. International Journal of Plasticity 20, 339 – 361.

Saai, A., Dumoulin, S., Hopperstad, O.S., Lademo, O.G., 2013. Simulation of yield surfaces for aluminium sheets with rolling and recrystallization textures. Computational Materials Science 67, 424 – 433.

Scipy, 2017. Optimization and root finding, Scipy version 1.0.0. URL: `https://docs.scipy.org/doc/scipy/reference/optimize.html`.

Shutov, A.V., Ihlemann, J., 2012. A viscoplasticity model with an enhanced control of the yield surface distortion. International Journal of Plasticity 39, 152 – 167.

Shutov, A.V., Panhans, S., Kreißig, R., 2011. A phenomenological model of finite strain viscoplasticity with distortional hardening. ZAMM - Journal of Applied Mathematics and Mechanics / Zeitschrift für Angewandte Mathematik und Mechanik 91, 653–680.

Spitzig, W.A., Richmond, O., 1984. The effect of pressure on the flow stress of metals. Acta Metallurgica 32, 457 – 463.

Stander, N., Roux, W., Basudhar, A., Eggleston, T., Goel, T., Craig, K., 2015. LS-OPT user's manual. Livermore Software Technology Corporation. Livermore, California, USA.

Steglich, D., Wafai, H., Besson, J., 2010. Interaction between anisotropic plastic deformation and damage evolution in Al 2198 sheet metal. Engineering Fracture Mechanics 77, 3501 – 3518.

Stout, M.G., Hecker, S.S., Bourcier, R., 1983. An evaluation of anisotropic effective stress-strain criteria for the biaxial yield and flow of 2024 aluminum tubes. Journal of Engineering Materials and Technology 105, 242–249.

Taylor, G.I., 1938. Plastic strain in metals. J. Inst. Metals 62, 307–324.

Teodosiu, C., Hu, Z., 1995. Evolution of the intragranular microstructure at moderate and large strains: Modelling and computational significance. Simulation of Materials Processing: Theory, Methods and Applications, Proceedings of the 5th International Conference on Numerical Methods in Industrial Forming Processes (NUMIFORM '95) 5, 173–182.

Vadillo, G., Fernández-Sáez, J., 2009. An analysis of gurson model with parameters dependent on triaxiality based on unitary cells. European Journal of Mechanics - A/Solids 28, 417 – 427.

Van Den Boogaard, T., Havinga, J., Belin, A., Barlat, F., 2016. Parameter reduction for the Yld2004-18p yield criterion. International Journal of Material Forming 9, 175–178.

Van Houtte, P., 1982. On the equivalence of the relaxed taylor theory and the bishop-hill theory for partially constrained plastic deformation of crystals. Materials Science and Engineering 55, 69 – 77.

Van Houtte, P., 1988. A comprehensive mathematical formulation of an extended taylor–bishop–hill model featuring relaxed constraints, the renouard–wintenberger theory and a strain rate sensitivity model. Texture, Stress, and Microstructure 8, 313–350.

Van Houtte, P., Delannay, L., Kalidindi, S.R., 2002. Comparison of two grain interaction models for polycrystal plasticity and deformation texture prediction. International Journal of Plasticity 18, 359 – 377.

Voce, E., 1948. The relationship between stress and strain for homogeneous deformation. J Inst Met 74, 537–562.

Wang, D.A., Pan, J., Liu, S.D., 2004. An anisotropic gurson yield criterion for porous ductile sheet metals with planar anisotropy. International Journal of Damage Mechanics 13, 7–33.

Wen, W., Borodachenkova, M., Tomé, C.N., Vincze, G., Rauch, E.F., Barlat, F., Grácio, J.J., 2015. Mechanical behavior of Mg subjected to strain path changes: Experiments and modeling. International Journal of Plasticity 73, 171 – 183.

Wen, W., Borodachenkova, M., Tomé, C.N., Vincze, G., Rauch, E.F., Barlat, F., Grácio, J.J., 2016. Mechanical behavior of low carbon steel subjected to strain path changes: Experiments and modeling. Acta Materialia 111, 305 – 314.

Westermann, I., Pedersen, K.O., Furu, T., Børvik, T., Hopperstad, O.S., 2014. Effects of particles and solutes on strength, work-hardening and ductile fracture of aluminium alloys . Mechanics of Materials 79, 58 – 72.

Wong, W.H., Guo, T.F., 2015. On the energetics of tensile and shear void coalescences. Journal of the Mechanics and Physics of Solids 82, 259 – 286.

Woodthorpe, J., Pearce, R., 1970. The anomalous behaviour of aluminium sheet under balanced biaxial tension. International Journal of Mechanical Sciences 12, 341 – 347.

Yoshida, F., Hamasaki, H., Uemori, T., 2013. A user-friendly 3D yield function to describe anisotropy of steel sheets. International Journal of Plasticity 45, 119 – 139.

Zhang, H., Diehl, M., Roters, F., Raabe, D., 2016. A virtual laboratory using high resolution crystal plasticity simulations to determine the initial yield surface for sheet metal forming operations. International Journal of Plasticity 80, 111 – 138.

Zhang, K., Holmedal, B., Hopperstad, O.S., Dumoulin, S., Gawad, J., Van Bael, A., Van Houtte, P., 2015. Multi-level modelling of mechanical anisotropy of commercial pure aluminium plate: Crystal plasticity models, advanced yield functions and parameter identification. International Journal of Plasticity 66, 3 – 30.

Zhang, K., Hopperstad, O.S., Holmedal, B., Dumoulin, S., 2014. A robust and efficient substepping scheme for the explicit numerical integration of a rate-dependent crystal plasticity model. International Journal for Numerical Methods in Engineering 99, 239–262.

Zhang, Z.L., Skallerud, B., 2010. Void coalescence with and without prestrain history. International Journal of Damage Mechanics 19, 153–174.